Symbolic Codes for Rotational Orbits

H. R. Dullin*
Department of Mathematical Sciences,
Loughborough University
Loughborough LE11 3TU, UK

J. D. Meiss and D. G. Sterling†
Department of Applied Mathematics
University of Colorado
Boulder, CO 80309-0526

March 30, 2022

Abstract

Symbolic codes for rotational orbits and "islands-around-islands" are constructed for the quadratic, area-preserving Hénon map. The codes are based upon continuation from an anti-integrable limit, or alternatively from the horseshoe. Given any sequence of rotation numbers we obtain symbolic sequences for the corresponding elliptic and hyperbolic rotational orbits. These are shown to be consistent with numerical evidence. The resulting symbolic partition of the phase space consists of wedges constructed from images of the symmetry lines of the map.

1 Introduction

Symbolic dynamics has been profitably used in the study of many dynamical systems since its invention by Hadamard in 1898 and naming by Morse and Hedlund in 1938 [1, 2, 3]. Among its many uses, symbolic dynamics can provide useful information about topological invariants such as the enumeration of periodic orbits and the entropy. It can also lead to numerical methods for finding periodic, homoclinic and chaotic orbits, and facilitate characterization of transport. Symbolic dynamics applies most directly to systems that are hyperbolic; indeed it was invented to describe geodesics on surfaces with negative curvature and famously applies to hyperbolic toral automorphisms and the Smale horseshoe.

In this paper we continue the study, began in [4], of the coding of orbits of Hénon's quadratic, area-preserving mapping [5]. Previously we used the concept of an anti-integrable (AI) limit [6] to define codes by continuation (see §2) and studied the bifurcations of homoclinic orbits that destroy the horseshoe of this map. In the current paper we study the codes of orbits that are born in rotational bifurcations of the elliptic fixed point. The rule that we obtain identifies the subset of orbits in the horseshoe that become rotational orbits, encircling the elliptic fixed point of the Hénon map.

The extension of symbolic dynamics to systems with stable orbits has proved difficult, except for the case of one-dimensional maps where classical results apply [7, 8]. The dissipative Hénon mapping [9] is a natural system to attempt the generalization of these results to multidimensional, nonhyperbolic systems, especially as it reduces (when $b = 0$) to the one-dimensional

*H.R.Dullin@lboro.ac.uk. Supported in part by DFG grant Du 302/2, and EPSRC grant GR/R44911/01.

†James.Meiss@Colorado.EDU, DSterling@somalogic.com. JDM was supported in part by NSF grant DMS-0202032, DGS was supported by an NRC postdoctoral fellowship.

logistic map. Just as the symbols for the logistic map are based on the itinerary of an orbit relative to the critical point, Grassberger and Kantz [10] proposed that the symbols for the Hénon map could be determined by partitioning the plane using the stable and unstable foliation and their "primary homoclinic tangencies," that is, points at which the local curvature of the unstable manifold diverges. This led to the concept of a "primary pruning front" in the symbol plane as determining the allowed sequences for a particular map [11]. Symbol sequences defined in this way can exhibit monodromy, that is, morph into new sequences on paths that encircle codimension-two bifurcations, such as a cusp [12]; along these paths, the primary tangencies may exhibit discontinuities [13]. As far as we know, this method has not been applied to the area-preserving case ($b = \pm 1$), though it has been applied to other dissipative systems, such as the cubic, generalized Hénon map [14].

Several other methods have also been proposed to obtain symbolic codes for orbits of the Hénon map. Biham and Wenzel defined the codes as the signature of a pseudo-gradient method for finding periodic orbits [15]. Sterling and Meiss proved that this technique works sufficiently close to an anti-integrable limit [16]. Unfortunately, it does not always converge to fixed points, and sometimes gives two codes for the same orbit [17]. Hansen and Cvitanovic defined codes by approximating the two-dimensional map near $b = 0$ by a sequence of one-dimensional unimodal maps [18]. The code defining an orbit can change if it crosses the critical point of one of the approximating maps.

Primary homoclinic tangencies have also been used to construct codes for the area-preserving standard map. For parameter values where elliptic periodic orbits and their associated islands are small (large k), Christiansen and Politi have shown that a primary set of homoclinic tangencies can be identified by their proximity to the dominant fold lines in the map [19]. Gaps between these points can be connected with symmetry lines associated with the reversibility of the map to form a curve that creates a symbol partition [20]. The symbol boundary can be modified to include elliptic islands, [21, 20], by choosing appropriate images of the symmetry lines. This method does not explain why symmetry lines are important, nor does it give a recipe for selecting the proper lines.

In §3 we give a rule for constructing the symbolic codes for orbits of the Hénon map with any given rotation number. These codes are consistent with those obtained by numerical continuation from the AI limit. We also show that these codes have definite symmetry properties, and that the symbolic partition in an elliptic island has the form of a wedge with apex at the elliptic fixed point and whose boundaries are constructed from specific symmetry lines. These wedges are similar to those found by Christiansen and Politi for the standard map.

Our rotational codes are closely related to those for maps with a natural angle variable, for example for circle maps [22, 23] and cat maps [24]. We review these ideas in the Appendices.

We also develop a systematic rule for obtaining the symbolic codes of rotational orbits with "higher class" [25], that is to "islands-around-islands," in §4-5. These correspond, for example, to orbits that rotate around orbits that rotate around the elliptic fixed point; thus they are defined by a sequence of rotation numbers. Our construction provides codes for the elliptic and hyperbolic orbits for each sequence of rotation numbers. Again the codes are shown to be consistent with the numerical evidence. The resulting symbolic partition is constructed from a sequence of wedges defined by symmetry lines.

A different method for constructing symbolic codes for islands-around-islands was given previously [26, 27]; however in these cases the entire set of orbits in an island was assigned the same sequence and the motivation was to study the transport implications for chaotic orbits outside the islands [25, 28].

2 Symbolic codes for the Hénon map by continuation

The area-preserving Hénon diffeomorphism can be written as[1]

$$(x, x') \mapsto f(x, x') = (x', -x - k + x'^2) \ . \tag{1}$$

An orbit of this map is written as a bi-infinite sequence $\mathcal{O} = (\ldots x_{-1}, x_0, x_1 \ldots)$ with $(x_{t+1}, x_{t+2}) = f(x_t, x_{t+1})$. The dynamics of this map exhibit the full range of behavior of typical area-preserving maps, including infinite cascades of period-doubling bifurcations, invariant circles, cantori, transport, twistless bifurcations, etc. [29, 30, 31]. As k increases, the dynamics become increasingly chaotic, and beyond a critical value, $k = k_H$, the set of bounded orbits forms a Smale horseshoe (this set has measure zero—almost all orbits escape to infinity). It was proved by Devaney and Nitecki that there is indeed a hyperbolic horseshoe when $k > 5 + 2\sqrt{5} > k_H$ [32, 16]. Our numerical studies indicate that [16, 4]

$$k_H \approx 5.699310786700 \ . \tag{2}$$

The dynamics of the bounded orbits in the hyperbolic horseshoe is conjugate to the full shift on two symbols. A simple way of constructing these symbols for the Hénon map is to define

$$s_t = \operatorname{sgn} x_t \tag{3}$$

because the bounded invariant set is divided by the coordinate axes, see Fig. 1.

An alternative method for obtaining these codes is to view the Hénon map as arising by continuation from an *anti-integrable* (AI) limit [6, 33]; for Eq. (1) we define

$$z = \epsilon x \ , \text{ with } \epsilon \equiv \frac{1}{\sqrt{k+1}} \ , \tag{4}$$

to rescale the map as

$$\epsilon(z_{t+1} + z_{t-1} - \epsilon) = z_t^2 - 1 \ .$$

To define ϵ, we assumed that $k > -1$, but this is not much of a restriction since there are no bounded orbits for the Hénon map when $k < -1$. The case $\epsilon \to 0$ is the AI limit [16, 4]. In this limit orbits reduce to sequences $z_t = \pm 1$, where the choice of sign is arbitrary—the map is equivalent to the full shift on the symbols $\pm$. Every such sequence continues away from the limit to an orbit of the Hénon map. Conversely, when there is a horseshoe these symbols agree with Eq. (3), and every bounded orbit of the Hénon horseshoe continues to an orbit at the AI limit.

Each point in the horseshoe is represented by a bi-infinite sequence of signs, together with the binary point representing the current position:

$$(x_t, x_{t+1}) \cong \mathbf{s} \equiv (\ldots s_{t-2}\, s_{t-1} \centerdot s_t\, s_{t+1} \ldots)$$

We denote the right-shift by σ, so that

$$\sigma\mathbf{s} = (\ldots s_{t-1}\, s_t \centerdot s_{t+1} \ldots) \tag{5}$$

When there is a hyperbolic horseshoe for $k > k_H$, the Hénon map f, restricted to the set of bounded orbits, is conjugate to the shift map σ acting on the sequence $\mathbf{s}$ that is the code for x.

[1] We do not use Hénon's original form, $(\xi, \eta) \to (1 - a\xi^2 + \eta, b\xi)$, since it becomes linear at $a = 0$, and is orientation-reversing for $b > 0$. Our form can be obtained by setting $b = -1$, and defining $k = a$, $x = k\eta$, and $x' = -k\xi$.

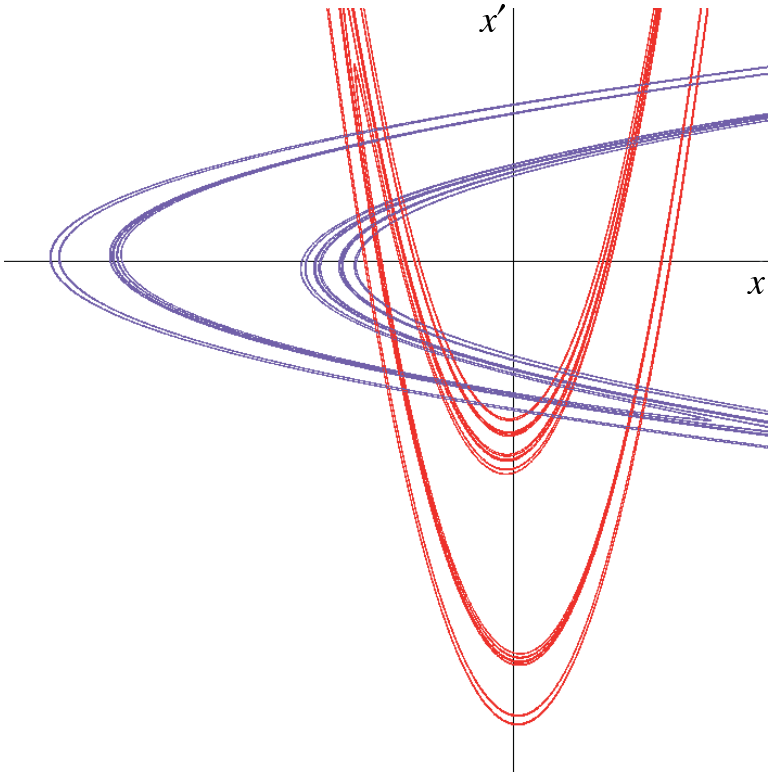

Figure 1: Stable (blue) and unstable (red) manifolds of the hyperbolic fixed point for the Hénon map when $k = 6$. The closure of the intersection of these manifolds is the horseshoe of bounded orbits.

We use continuation away from the AI limit to find orbits with a given code as k varies [16]. Such a "global coding" is complete if every smooth one-parameter family in the extended space $\mathbb{R}^2 \times \mathbb{R}$ (phase space times parameter) connects to the AI limit. Because of twistless bifurcations it is not enough to simply take the map parameter k as a family parameter [31, 4]. We do not know any counterexample to this "smooth no-bubble conjecture", and adopt it as our working hypothesis.

We use the signs $+$ and $-$ to denote the symbols s_t. For example the hyperbolic fixed point, at $x_t = 1 + \sqrt{1+k}$, has code $s_t = +$; we denote the bi-infinite sequence for this orbit by $\mathbf{s} = (+)^\infty$. In general a period-n orbit is given by the bi-infinite concatenation of a sequence of n symbols; we represent this with a superscript ∞: $(s_0\, s_1\, \ldots\, s_{n-1})^\infty$. We often denote repeated symbols with a superscript, thus $(-+^7)^\infty$ is a period-8 orbit. The *parity* of a finite symbol sequence is defined to be the product of its symbols:

$$\pi(s_0 s_1 \ldots s_{n-1}) = \prod_{t=0}^{n-1} s_t \ . \tag{6}$$

Equivalently the parity is *even* or *odd* if the number of minus signs is as well. A parity can be assigned to any periodic orbit by computing the parity of its fundamental sequence; for example, $\pi((-++{+})^\infty) = -1$.

Using the continuation method, we can follow orbits from the AI limit to visualize the relation between the symbolic codes and the positions of the corresponding points in phase space. If we distinguish points solely by a single symbol, s_0, this gives a partition of the phase space into regions corresponding to the $+$ and the $-$ code. Using the conjugacy between the shift σ and

the Hénon map on these orbits, we could reconstruct the full symbol sequence for each orbit by following the sequence of visits to the two elements of the partition.

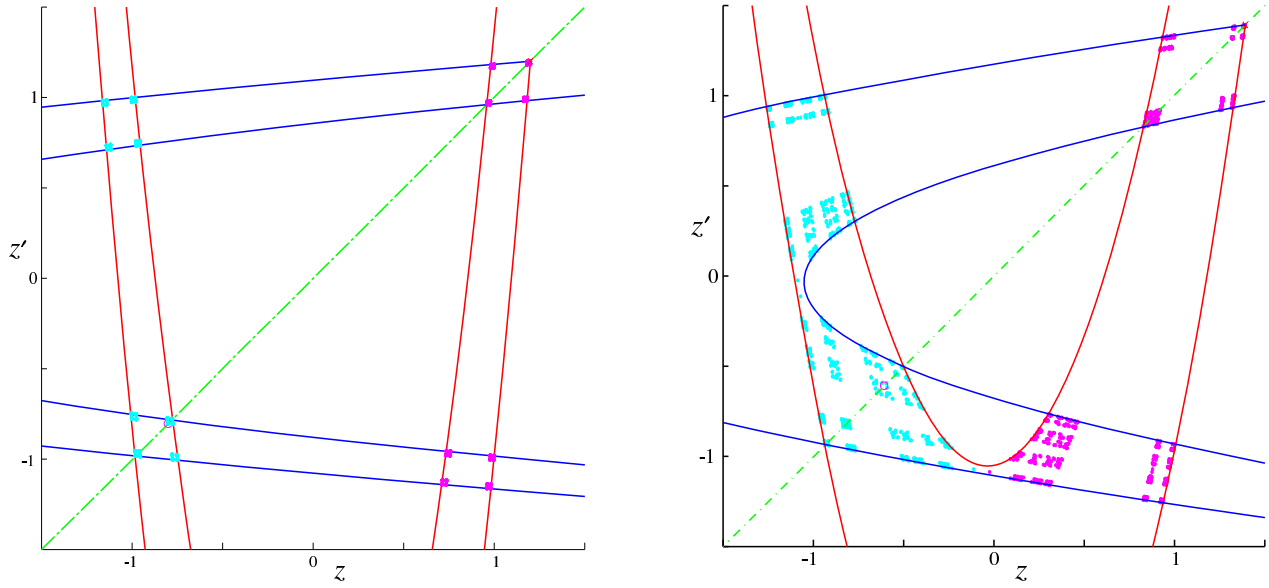

Figure 2: Points on the 99 periodic orbits of the Hénon map with periods up to 10 for two different parameter values. In the left panel $k = 24$ ($\epsilon = 0.2$) and in the right $k = 5.5$ ($\epsilon \approx 0.392$). The blue (red) curves are the initial lobes of the stable (unstable) manifolds for the hyperbolic fixed point, $(+)^\infty$, located in the upper right corner.

In Fig. 2, a point is colored cyan if $s_0 = -$, and magenta if $s_0 = +$. We use the scaled coordinates (z, z'), defined in Eq. (4) for the plots, so that as $k \to \infty$ all bounded orbits converge to the four AI states $(z, z') = (\pm 1, \pm 1)$. As k decreases the trajectories move away from these points as shown in the left frame of Fig. 2. For this value of ϵ it can be proven that all of the trajectories reside within the union of four small squares with sides $M_\infty \approx 0.568$ that are centered on the four AI states [16]—actually we observe that they are contained in smaller rectangles bounded by segments of the stable and unstable manifolds of the hyperbolic fixed point. These segments intersect at points on the "type one" homoclinic orbits with symbol sequences $+^\infty . -(-) - +^\infty$ and $+^\infty . -(+) - +^\infty$ [4]. As ϵ increases the bounded orbits move further from the AI states, and the stable and unstable manifolds of $(+)^\infty$ approach their first tangency. Just below $k = k_H$ (right panel of Fig. 2) the two type-one homoclinic orbits have been destroyed in a homoclinic bifurcation and only a subset of symbol sequences are now allowed. Nevertheless, the symbol boundary is still very simple (at least up to this period), and is delineated by the near tangency between the first lobes of the stable and unstable manifolds.

One phenomenon special to area-preserving maps is the existence of elliptic periodic orbits. For example, the second fixed point, $(-)^\infty$ (at $x_t = 1 - \sqrt{1+k}$) becomes elliptic at $k = 3$. More generally this orbit has positive *residue* for any $k > -1$. Recall that Greene's residue, r, is a convenient encoding for the linear stability of an orbit of an area-preserving map: given a point (x, x') on a period-n orbit of f, then

$$r \equiv \frac{1}{4}(2 - \mathrm{Tr}(Df^n(x, x')) \tag{7}$$

Orbits are elliptic when $0 < r < 1$, hyperbolic when $r < 0$ and reflection hyperbolic when $r > 1$. For example, the fixed point $(-)^\infty$ is elliptic for $-1 < k < 3$ and at $k = 3$ undergoes a

period-doubling bifurcation becoming hyperbolic with reflection. More generally [4] for a period n orbit, as $k \to \infty$,

$$r \sim -\pi(\mathbf{s})\frac{1}{4}(4k)^{n/2} \ . \tag{8}$$

Thus the parity of a symbol sequence determines the character of the orbit for large k. Often, we refer to orbits that are born with positive residue as "elliptic" even though they typically undergo bifurcations that destroy their stability and may even smoothly continue to orbits with negative residue.

Our goal for this paper is to investigate the structure of the symbol partition when there are elliptic periodic orbits and their associated rotational orbits. In particular, Fig. 3 shows that the symbol boundary near an elliptic orbit exhibits a structure radically different from the horseshoe shown in Fig. 2. In the following sections, we will explain the wedge shaped symbol boundary that eminates from the elliptic fixed point in Fig. 3. To do this, we must construct the codes for rotational orbits.

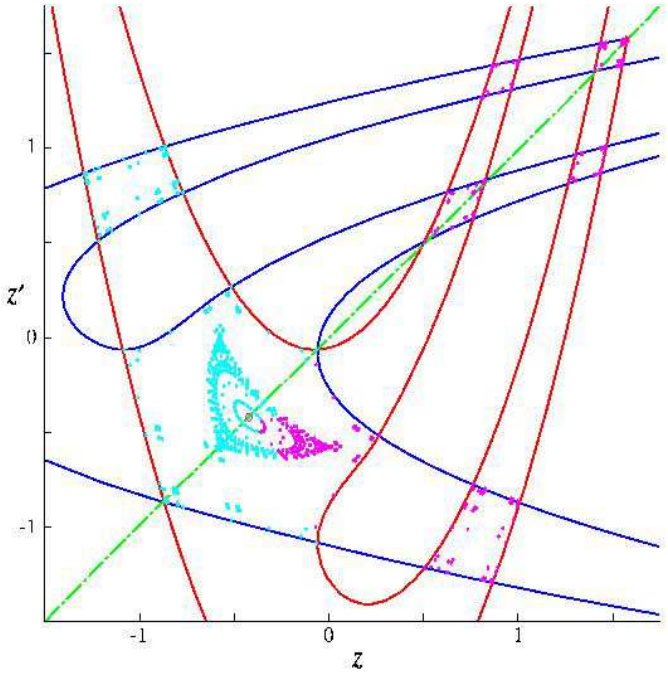

Figure 3: Periodic orbits of the Hénon map for $k = 2.0$. Plotted are points on all periodic orbits up to period 10 that still exist, as well as all rotational (class-one) orbits with periods up to 31 that exist at this parameter value. Points with $s_0 = +$ $(-)$ are colored magenta (cyan). It is apparent that the first few lobes of the stable and unstable manifolds no longer delineate the symbol boundary in the vicinity of the elliptic fixed point.

3 Rotational (Class-One) Orbits

One special class of orbits for the Hénon map are the *rotational* orbits—those that are created by a rotational bifurcation of the elliptic fixed point $(-)^\infty$. Generally, a rotational bifurcation occurs when the linearized rotation number at an elliptic fixed point passes through a given

rotation number $0 \le \omega \le \frac{1}{2}$, i.e., when

$$r = \frac{1}{4}(2 - e^{2\pi i\omega} - e^{-2\pi i\omega}) = \sin^2(\pi\omega) \tag{9}$$

Since the residue of the elliptic fixed point is $r((-)^\infty) = \frac{1}{2}\sqrt{1+k}$, we can solve Eq. (9) for k or ω to obtain

$$\begin{aligned} k(\omega) &= \cos(2\pi\omega)(\cos(2\pi\omega) - 2) \\ \omega(k) &= \frac{1}{\pi}\arcsin\left(\frac{(1+k)^{1/4}}{\sqrt{2}}\right) . \end{aligned} \tag{10}$$

Since the residue of a period-n orbits grows like $k^{n/2}$ as $k \to \infty$ it is more convenient for numerical work to use the scaled residue

$$\rho \equiv \frac{1}{\sqrt{k+1}}\,\mathrm{sgn}(r)\,[4|r|]^{1/n} . \tag{11}$$

Notice $\rho = 0 \Leftrightarrow r = 0$, and as $k \to \infty$, Eq. (8) implies that $\rho \to \pm 2$.

When $\omega(k)$ is rational, a rotational bifurcation typically[2] creates a pair of orbits, one elliptic and one hyperbolic, we call these *class-one* rotational orbits following Meiss [25] (the two fixed points are therefore class-zero orbits). A theorem of Franks implies that there are class-one period q orbits for each rational rotation number p/q whenever $0 < p/q < \omega(k)$ [35]. Each elliptic class-one periodic orbit is typically encircled by rotational orbits of class-two, giving rise to "island chains." We will discuss these higher class orbits in §4. When $\omega(k)$ is irrational and Diophantine, Moser's twist theorem implies that the rotational bifurcation gives birth to an invariant circle [36]. If $\omega(k)$ is not sufficiently irrational, we expect that a cantorus is born (as indicated by Aubry-Mather theory, though we know of no proof of this for the Hénon map).

We begin this section with some observations from our numerical experiments. We then construct a rule that generalizes these observations and appears to be consistent with all class-one orbits. This construction has a natural geometric interpretation in terms of circle maps. The code that we obtain is related to that for rotational orbits in other systems, for example the codes obtained for minimizing rotational orbits in twist maps by Aubry [37], for cat maps by Percival and Vivaldi [24], billiards by Bäcker and Dullin [38], and for circle maps by Lin [3]. We discuss some of these relationships in the Appendices.

3.1 Preliminary Numerical Observations

It was not obvious to us which of the possible period-n orbits at the AI limit should be identified as the class-one rotational orbits. Thus we began by searching for periodic codes that continue to orbits that collide with $(-)^\infty$ at $k(\omega)$ defined by Eq. (10). A brute force way to systematically search for rotational orbits, would be to choose a period and continue *all* periodic codes of that length from the AI limit until the corresponding orbits bifurcate. For example, at period 4 there are three distinct periodic codes: $(---+)^\infty, (--++)^\infty$, and $(-+++)^\infty$. Upon continuation, we discover that the orbits corresponding to $(--++)^\infty$ and $(-+++)^\infty$ collide when $k = k(\frac{1}{4}) = 0$ at the position of the elliptic fixed point. These two orbits have negative and positive residues, respectively (in agreement with Eq. (8)) during their entire lifetimes, and thus they represent the hyperbolic and elliptic $\frac{1}{4}$ orbits. In our previous numerical experiments,

[2]When the period is larger than four. The tripling and quadrupling bifurcations are special, see e.g. [34].

we followed each of the 1.47 million orbits of the Hénon map with periods up to 24 in order to obtain a numerical estimate of the parameter at which the Hénon map horseshoe is destroyed [4].

We can actually considerably reduce the number of sequences that need to be checked by computing the rotation number of the symbol sequence using the "self-rotation number" [39]. The self-rotation number of symbol sequence is the same as that of the orbit, and is unchanged as k varies. As shown in Table 2 of [39] the self-rotation number of $(---+)^\infty$ is $\frac{1}{2}$, thus it cannot be one of the rotational period-four orbits—indeed it arises in a period-doubling bifurcation of the period-two orbit, $(-+)^\infty$.

Proceeding in this way we identified all of the class-one rotational orbits with periods less than 20 [40]. There are 118 such orbits; the first few of these are shown in Table 1. In the table we chose a canonical permutation to order these sequences (we will discuss the canonical ordering in §3.2).

Our numerical observations indicate that all of the class-one rotational orbits smoothly continue to the AI limit; we know of no proof of this observation. We observe that the codes for the negative and positive residue orbits differ only in one symbol, the second: indeed, this symbol is simply the sign of the residue, indicated by a $*$ in the symbol sequence.

At this point the pattern for the rotational codes that we will describe in the next section became clear.

3.2 Rotational Codes

Since the dynamics on a smooth invariant circle with irrational rotation number ω is conjugate to a rigid rotation with this rotation number, it is natural to construct a symbolic code for rotational orbits based this conjugacy. Letting θ denote a point on the circle with unit circumference, the rigid rotation is

$$\theta \mapsto \theta + \omega \mod 1 \quad \Rightarrow \quad \theta_t = \{\omega t + \alpha\} \,, \tag{12}$$

where α is the initial phase. Here $\{x\} \equiv x - \lfloor x \rfloor$ denotes the fractional part of x, and $\lfloor x \rfloor \equiv \max_{p\in\mathbb{Z}}\{p : p \le x\}$ is the *floor* function. To agree with our sign choice in Eq. (1), we will depict this as a clockwise rotation, see Fig. 4.

To obtain the codes for the circle map, divide the circle into two wedges

$$\begin{aligned} W_-(\omega) &= (-\omega, \omega) \\ W_+(\omega) &= [\omega, 1-\omega] \,, \end{aligned} \tag{13}$$

see Fig. 4. Note that $W_-(\omega)$ is open and $W_+(\omega)$ is closed, and that these wedges divide the circle into two parts for any $0 < \omega \le \frac{1}{2}$.

Definition 1 (Rotational (class-one) Code). *A point $\theta \in W_s(\omega)$ is defined to have symbol s. The code for the rotational orbit $\theta_t = \omega t + \alpha$ is*

$$s_t = \pm \quad \textit{when} \quad \theta_t \in W_\pm(\omega) \,. \tag{14}$$

There are two distinct types of codes that we distinguish by the value of the initial phase α. When $\alpha = 0$, the first two symbols of the code are always $-+$ while if $\alpha \in (-\omega, 0)$ then they are $--$. Indeed, if $\alpha \neq \{j\omega\}$ for any integer j, then the symbol $-$ always appears doubled in the code.[3] To distinguish these two cases, we call the case that $\alpha \neq \{j\omega\}$ for some $j \in \mathbb{Z}$ a *hyperbolic*-code, and the alternative case an *elliptic*-code.

[3]For hyperbolic codes for rational ω this is Lemma 6.11 in [40].

ω	Code	$k(\omega)$	PD
$\frac{0}{1}$	$(*)^\infty$	-1	3
$\frac{1}{2}$	$(-+)^\infty$	3	4
$\frac{1}{3}$	$(-*+)^\infty$	$\frac{5}{4}$	$\frac{5}{4}$
$\frac{1}{4}$	$(-*++)^\infty$	0	0.2174036214†
$\frac{1}{5}$	$(-*+++)^\infty$	$\frac{7-5\sqrt{5}}{8}$	-0.2404626622*
$\frac{2}{5}$	$(-*--+)^\infty$	$\frac{7+5\sqrt{5}}{8}$	2.822983929*
$\frac{1}{6}$	$(-*+^4)^\infty$	$-\frac{3}{4}$	-0.4766507416
$\frac{1}{7}$	$(-*+^5)^\infty$	-0.8582400707	-0.6124008240
$\frac{2}{7}$	$(-*+--++)^\infty$	0.4945574340	0.7226142786
$\frac{3}{7}$	$(-*-^4+)^\infty$	2.613682637	3.099045238
$\frac{1}{8}$	$(-*+^6)^\infty$	$\frac{1}{2}-\sqrt{2}$	-0.6974167690
$\frac{3}{8}$	$(-*---+--+)^\infty$	$\frac{1}{2}+\sqrt{2}$	2.4246586398
$\frac{1}{9}$	$(-*+^7)^\infty$	-0.9452647974	-0.7546238304
$\frac{2}{9}$	$(-*++--+++)^\infty$	-0.3171426657	-0.0739574299
$\frac{4}{9}$	$(-*-^6+)^\infty$	2.762407463	3.187557989
$\frac{1}{10}$	$(-*+^8)^\infty$	$\frac{-1-3\sqrt{5}}{8}$	-0.7954212145
$\frac{3}{10}$	$(-*+--+--++)^\infty$	$\frac{-1+3\sqrt{5}}{8}$	0.8673114431
$\frac{1}{11}$	$(-*+^9)^\infty$	-0.9747995591	-0.8258655309
$\frac{2}{11}$	$(-*+++--+^4)^\infty$	-0.6582603930	-0.4217831728
$\frac{3}{11}$	$(-*+--++--++)^\infty$	0.3048831897	0.5506136016
$\frac{4}{11}$	$(-*--+--+--+)^\infty$	1.738564049	2.225483132
$\frac{5}{11}$	$(-*-^8+)^\infty$	2.839612714	3.215096092
$\frac{1}{12}$	$(-*+^{10})^\infty$	$\frac{3}{4}-\sqrt{3}$	-0.8493921692
$\frac{5}{12}$	$(-*-^4+-^4+)^\infty$	$\frac{3}{4}+\sqrt{3}$	2.908515654

† The smaller real root of $16k^4-64k^3-8k^2+1$

* The two real roots of $4096k^6-13312k^5+512k^4+17344k^3-7520k^2-16276k-3251$

Table 1: Codes for class-one rotational orbits. The $*$ represents $\pm$ for positive and negative residue orbits, respectively. The third column is the value Eq. (10) at which the orbits collide with $(-)^\infty$ in a rotational bifurcation. The column "PD" is the value of k for which the positive residue orbits undergo period-doubling. The elliptic $\frac{1}{3}$ and $\frac{3}{10}$ orbits actually are created earlier in saddle-center bifurcations at $k=1.0$ and $k=0.7063926$, respectively.

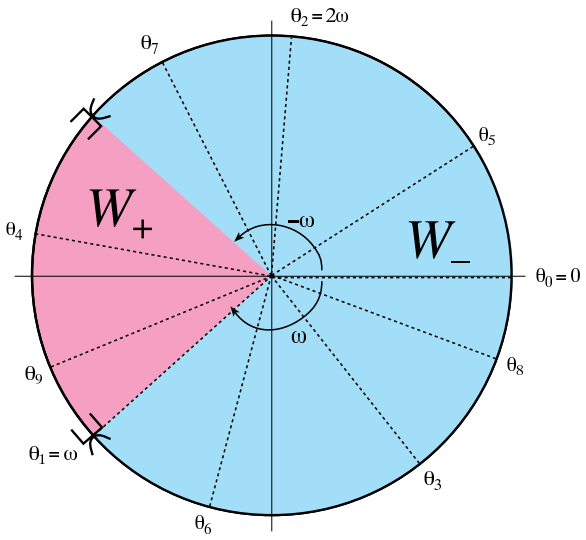

Figure 4: Construction of the rotational code for $\omega = \gamma^{-2}$ (where γ is the golden mean) using the wedges $W_{\pm}(\omega)$. The orbit shown corresponds to the elliptic code with $\alpha = 0$.

Note that whenever $\omega \neq \frac{1}{2}$ there are at least two distinct codes. For example if we set $\omega = \frac{1}{3}$, then the three possible elliptic codes are $-++$, $+-+$ and $++-$, all of which represent the same periodic orbit with code, $(-++)^{\infty}$. Similarly all the hyperbolic codes are cyclic permutations of $(--+)^{\infty}$. In the exceptional case, $\omega = \frac{1}{2}$, there is only one period-two code, the elliptic code, $(-+)^{\infty}$.[4]

It is easy to see that a hyperbolic code consists of blocks of the form $--+^{m-2}$ and $--+^{m-1}$, where $m = \lfloor \omega^{-1} \rfloor$, For example, denoting the golden mean by $\gamma \equiv \frac{1+\sqrt{5}}{2}$, then $\omega = \gamma^{-2} \approx 0.381966011$. Therefore $\gamma^{-2} \in (\frac{1}{3}, \frac{1}{2})$ and $m = 2$, so that the code is built from the blocks $--$ and $--+$. For example if we choose $\alpha = -.1$, we obtain

$$(\ldots - - - - - + \cdot - - - - - + - - + - - - - - + - - - - - + - - + - - - - - + - - + - \ldots)$$

For irrational ω there are infinitely many hyperbolic codes, depending upon the choice of α. By contrast, there is only one elliptic code, up to cyclic permutations, because any choice $\alpha = j\omega$ generates the same sequence of symbols. When $\alpha = 0$ the elliptic code for $\omega = \gamma^{-2}$ is

$$(\ldots + - - + \cdot - + - - + - - - - + - - + - - - - + - - - - + - - + - - - - + \ldots),$$

in agreement with the first few points shown in Fig. 4. As previously asserted the "first" two symbols in this code are $-+$, but all other blocks have an even number of $-$'s.

When ω is rational, Def. 1 gives rise to exactly two distinct codes (up to cyclic permutation). As we will see, these correspond to the two class-one orbits with this rotation number.

Lemma 1. *For any rational rotation number in* $(0, \frac{1}{2})$*, there are exactly two codes (the elliptic and hyperbolic codes) up to cyclic permutations.*

Proof. Set $\omega = \frac{p}{q}$, where $p, q \in \mathbb{Z}$ are relatively prime. The periodic orbit consists of q evenly spaced points on the circle, and subsequent points are obtained by shifting p points around the circle. Partition the circle into q half-open sectors

$$S_j = (\frac{j}{q}, \frac{j+1}{q}], \; j = 0, 1, \ldots q-1 \; . \tag{15}$$

[4]This agrees with the fact that the Hénon map also has only one period-2 orbit.

Then each S_j contains exactly one point of the orbit. Note that W_- consists of the interior of the union of $2p$ of the S_j

$$W_- = \mathrm{Int} \bigcup_{j=-p}^{p-1} S_j \ ,$$

(where the indices are taken mod q) and the interior of W_+ is the union of the remaining ones

$$\mathrm{Int}\, W_+ = \mathrm{Int} \bigcup_{j=p}^{q-p-1} S_j \ .$$

It is immediately clear that each orbit with $\alpha \in \mathrm{Int}\, S_0$ has the same (hyperbolic) code, since the points fall in the interiors of exactly the same sequence of S_j, and therefore in the same sequence of W_i. Similarly, for any j, the codes for orbits that have $\alpha \in \mathrm{Int}\, S_j$ are all identical. Finally since an orbit that starts in the interior of S_0 reaches S_j after some number, t, steps, then the codes of orbits that start in these two sectors are the same up to cyclic permutation.

For the elliptic case we set $\alpha = j/q$ for integer $0 \le j < q$. Each of these orbits corresponds to the same set of points on the circle (the boundary points of the S_j), differing only by cyclic permutation. Thus their codes also differ only by cyclic permutation.

Finally the elliptic code has only $2p-1$ points in $W_-(\omega)$, while the hyperbolic code has $2p$ points. Thus these two codes differ. □

We choose a canonical ordering for these two codes by selecting $\alpha = 0$ for the elliptic case and $\alpha = -\frac{1}{2q}$ for the hyperbolic case (this mimics the interleaving of the two orbits of an island chain). Thus the elliptic code always starts with $-+$ and the hyperbolic with $--$. From the third symbol onwards the two codes are identical.

Lemma 2 (Properties of Rotational Codes). *The canonically ordered elliptic and hyperbolic codes for periodic orbits differ only in their second symbol: $s_1 = -$ for hyperbolic and $s_1 = +$ for elliptic codes. Elliptic codes have odd parity and hyperbolic codes have even parity.*

Proof. This follows immediately from the fact that both orbits initially lie in the sector S_{q-1} defined in the previous lemma. Thus they visit exactly the same sectors in the same order. The only symbolic difference occurs at $t = 1$ where the elliptic point lies at $\theta_1 = \omega \in W_+$, while the hyperbolic point is in the interior of S_{p-1}, which is in W_-. The elliptic code has odd parity since it has exactly $2p-1$ points in W_-. □

A convenient representation for rotational codes is the Farey tree, Fig. 5. The tree shows that the canonical hyperbolic code of a Farey daughter is simply the concatenation of the codes of its hyperbolic parents (putting the code from the larger rotation number on the left). This fact is proved in Appendix A.3.

As we will see in §3.5, the wedge shaped symbol boundaries in Fig. 4, translate into a similar wedge for the symbol boundary in the phase space of the Hénon map. However, before examining this, we present additional numerical evidence that lead to Def. 1.

3.3 Numerical Observations

While there is no proof that the codes for the rotational orbits of the Hénon map are generated by Eq. (14), we conjecture that this is the case:

Conjecture 1. *Every class-one rotational orbit of the area-preserving Hénon map smoothly continues to an orbit of the horseshoe with code defined by Eq. (14).*

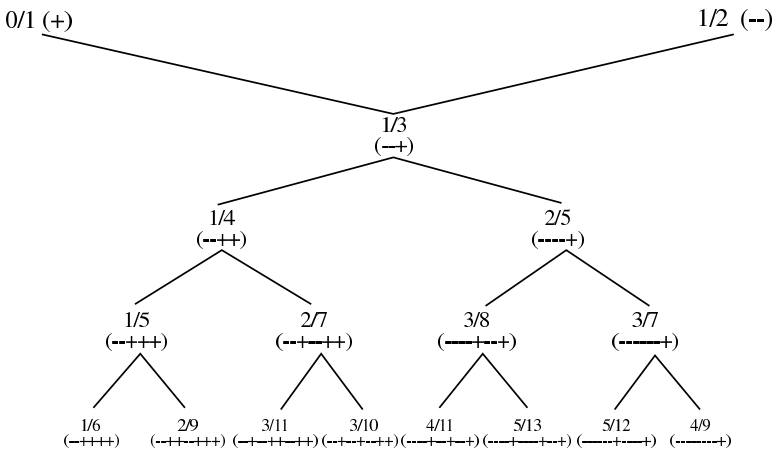

Figure 5: Farey tree for the base $\frac{0}{1}$ and $\frac{1}{2}$ up to level three, and the corresponding codes for the hyperbolic rotational orbits. The code for $\frac{1}{2}$ does not correspond to a real orbit, as there is no "hyperbolic" period-two orbit. The codes for the elliptic rotational orbits are obtained by flipping the second symbol.

As noted in §3.1, our initial observations indicate that this conjecture is true up to period 20. In this section we show in addition that Eq. (14) generates the correct codes for all rotational orbits up to period 99; i.e., that these orbits are born in a rotational bifurcation of elliptic fixed point at the value of k given by Eq. (9). To test this we must numerically continue each such orbit to parameter value where its residue vanishes. We observe that each hyperbolic rotational orbit has a negative residue near the AI-limit, and that r monotonically increases as k decreases until it reaches zero at a rotational or saddle-center bifurcation. Similarly elliptic rotational orbits have positive residues near the AI-limit, and r monotonically decreases to zero as k decreases. In Fig. 6 we show the scaled residue, Eq. (11), as a function k for five elliptic and hyperbolic class-one orbits.

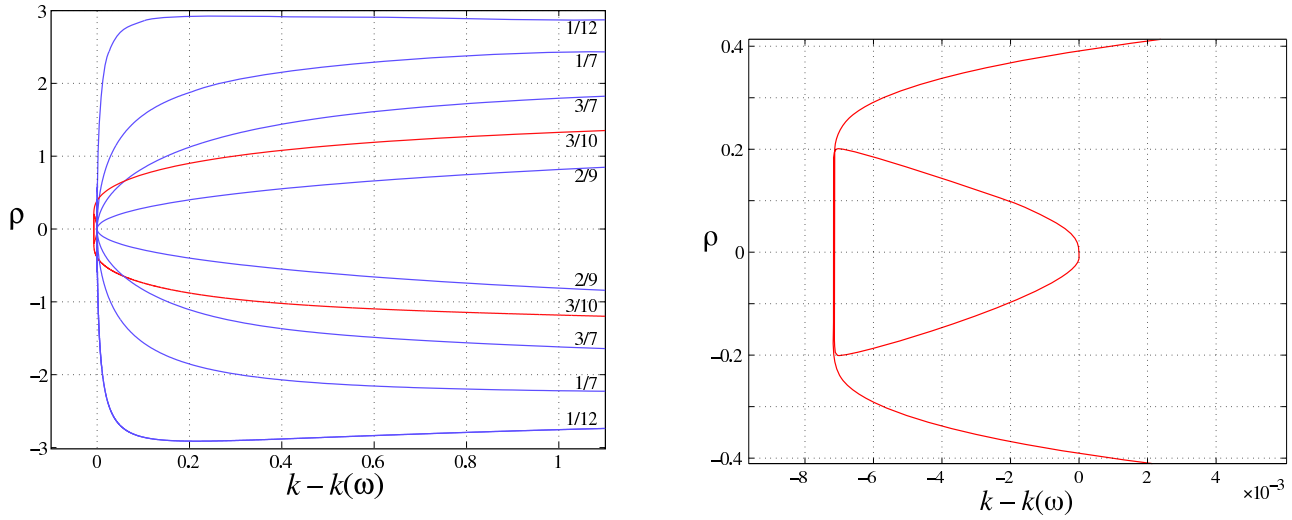

Figure 6: Left Panel: Scaled residue Eq. (11) as a function of the deviation k from $k(\omega)$ for 5 class-one rotational orbits. Right panel: an enlargement of the residue for the $\omega = \frac{3}{10}$ orbit in the vicinity of the rotational and twistless bifurcations.

Thus it would appear that a quick method for detecting the rotational bifurcation would be

to find the parameter value, $k_1(\omega)$ for the first zero of r moving away from the AI limit. In Fig. 7 we plot the number of digits of agreement between $k_1(\omega)$ and $k(\omega)$ for the 1501 class-one rotational orbits up to period 99 as a function of rotation number. This shows that the first zero crossing of r corresponds to the rotational bifurcation for most of the orbits. The dashed curve in the right hand pane of the figure shows the cumulative distribution function for the precision data for the complete set of 1501 orbits. There are two groups of orbits for which the apparent precision is lower than 7 digits.

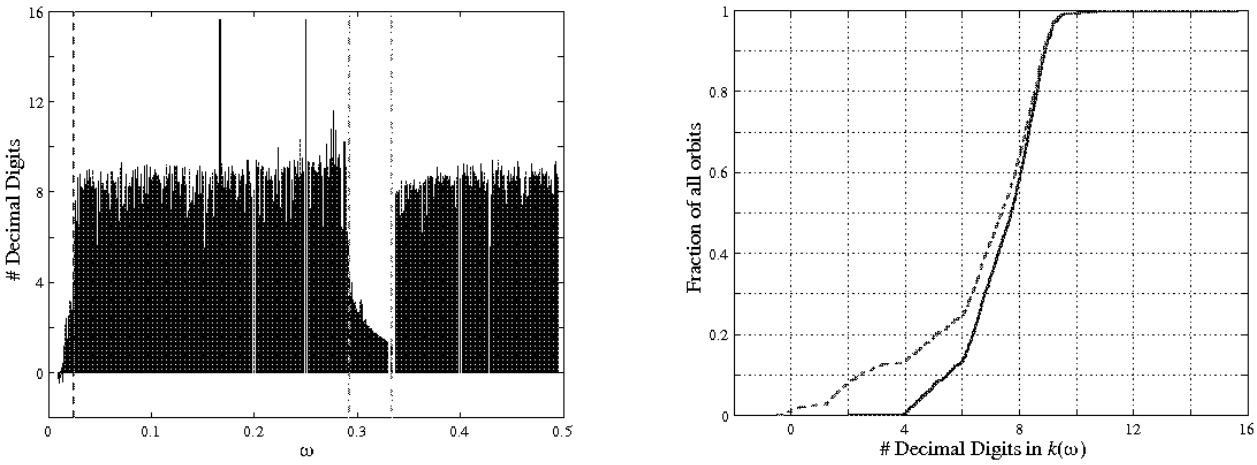

Figure 7: Left Panel: Plot of $-\log_{10}(k_1(\omega) - k(\omega))$ for the 1501 class one rotational orbits with periods up to 99. The right panel shows the distribution of digits of precision in the 1501 numerical bifurcation values (dashed line), and 1305 values for orbits with $\omega > 0.025$ and either $k(\omega) < \frac{9}{16}$ or $k(\omega) > \frac{5}{4}$ (solid line). The latter case are the class-one orbits created at parameter values where the Hénon map has twist and the rotation frequency is large enough to avoid numerical difficulties.

One of these groups corresponds to orbits with $\omega \in [0.29021, \frac{1}{3}]$, shown by the (green) dashed lines in Fig. 7. This rotation number interval corresponds to the parameter interval $\frac{9}{16} < k < \frac{5}{4}$ where the twist of the Hénon map is "anomalous" [31]. By "normal" twist we mean that the rotation number decreases monotonically moving away from the elliptic fixed point. In the anomalous interval the rotation number increases near the elliptic point before reaching a maximum and eventually decreasing. For orbits in this interval the first zero of the residue corresponds to a saddle-node bifurcation at $k_1(\omega) < k(\omega)$. For example, in the right panel of Fig. 6 we show an enlargement of the scaled residue plot for the $\frac{3}{10}$ orbits. For this case, the first zero crossing along the curve from the AI limit occurs at $k \approx 0.7063832$ for the hyperbolic orbit and $k \approx 0.7063926$ for the elliptic orbit (these points are almost indistinguishable in the figure). The rotational bifurcation (which is the reference value in Fig. 7) corresponds to the second zero crossing along each curve; this occurs at $k(3/10) \approx 0.7135255$. This explains the apparent loss in accuracy in the second interval (bounded by the green dashed lines) in Fig. 7.

Our continuation method could not find the bifurcation values for orbits with $\omega < \frac{1}{41}$ (indicated by the (red) dashed line in Fig. 7) to more than 4 digits. This is due to the ill-conditioning of the equations as $k \to -1$. In this region the elliptic and hyperbolic fixed points approach one another and the map is nearly integrable. This is reflected in the fact that periodic orbits very nearly lie on periodic invariant circles and so there is nearly a null direction in the matrices used in the continuation method. Our numerical method fails when the condition number of the matrices exceeds 10^{12}, and for low frequency rotational orbits the onset of this ill-conditioning occurs much further from the bifurcation value than for higher frequency orbits. This causes a

premature loss of precision and produces less accurate estimates of the bifurcation values.

The solid curve in the right hand pane of Fig. 7 shows the cumulative precision data for the subset of orbits with $\omega \geq 0.025$ and either $k(\omega) < \frac{9}{16}$ or $k(\omega) > \frac{5}{4}$. The continutation method produced at least 7 digits of precision for 70% of of the orbits; none of the obits had fewer than 4 digits of precision once we excluded the orbits with anomalous twist and low frequencies. In every case that we investigated, the precision can be improved by carefully "hand-tuning" the parameters of the continuation method (in particular the parameters in the variable step-size routines). Thus we believe that Fig. 7 gives compelling evidence in favor of Conjecture 1.

3.4 Symmetry

As is well-known [41], the area-preserving Hénon map is reversible; that is, it is conjugate to its inverse $f \circ S = S \circ f^{-1}$, where

$$S(x, x') = (x', x) \ . \tag{16}$$

Note that the reversor S is orientation reversing, $\det(DS) = -1$, and is an involution, $S^2 = id$. Whenever a map is reversible in this sense, it can be factored into a pair of orientation-reversing involutions, $f = (fS) \circ S = R \circ S$. The second reversor for Eq. (1) is

$$R(x, x') = (x, -x' - k + x^2) \ . \tag{17}$$

More generally, any image of a reversor is also a reversor; the full set of involution pairs $\{(f^j R, f^j S), j \in \mathbb{Z}\}$ form a *family* of reversors. Thus for example,

$$T(x, x') \equiv f^{-1} S(x, x') = Sf(x, x') = (-x - k + x'^2, x') \tag{18}$$

is also a reversor, and since $f^{-1}R = S$, we have $f = ST$. We will sometimes find it convenient to use this alternative factorization.

An orbit $\mathcal{O}$ is *symmetric* if it is invariant under a reversor, that is if $S\mathcal{O} = \mathcal{O}$. It is easy to see that every symmetric periodic orbit has two points on the fixed sets of S or R [41]; we denote these, for example, as $\mathcal{S} = \mathrm{fix}(S) = \{(x, y) : S(x, y) = (x, y)\}$:

$$\begin{aligned} \mathcal{S} &= \{(x, x') : x = x'\} \ , \\ \mathcal{R} &= \{(x, x') : 2x' = x^2 - k\} \ . \end{aligned} \tag{19}$$

The fixed set of T is related to Eq. (19) because $f^n \mathcal{R} = \mathrm{fix}(f^{2n} R)$, which implies that

$$f^{-1}\mathcal{R} = \mathcal{T} = \{(x, x') : 2x = x'^2 - k\} \ .$$

The fixed sets intersect at the elliptic and hyperbolic fixed points. Following [25], we divide the lines at the elliptic fixed point, labeling the four rays with a subscript i for the *ingoing* half of the line (leading to the hyperbolic point) and subscript o for the *outgoing* half (leading away to infinity). An example is shown in Fig. 8 for $k = 2.75$, where the hyperbolic fixed point is off-scale (to the upper right), and the elliptic fixed point is centered. Shown are a number of class-one invariant circles and periodic orbits that have class-two invariant circles around them. Each of the class-one periodic orbits is symmetric; for example, the $\frac{3}{7}$ elliptic orbit has points on $\mathcal{R}_o$ and $\mathcal{S}_i$, while its hyperbolic partner has points on the other two rays.

It was first noted by Greene that for many reversible examples the class-one, elliptic, rotational periodic orbits tend to lie on one particular symmetry ray, called the dominant ray [29, §1.2.3]. To our knowledge this has never been proven in general, though it is known to be true

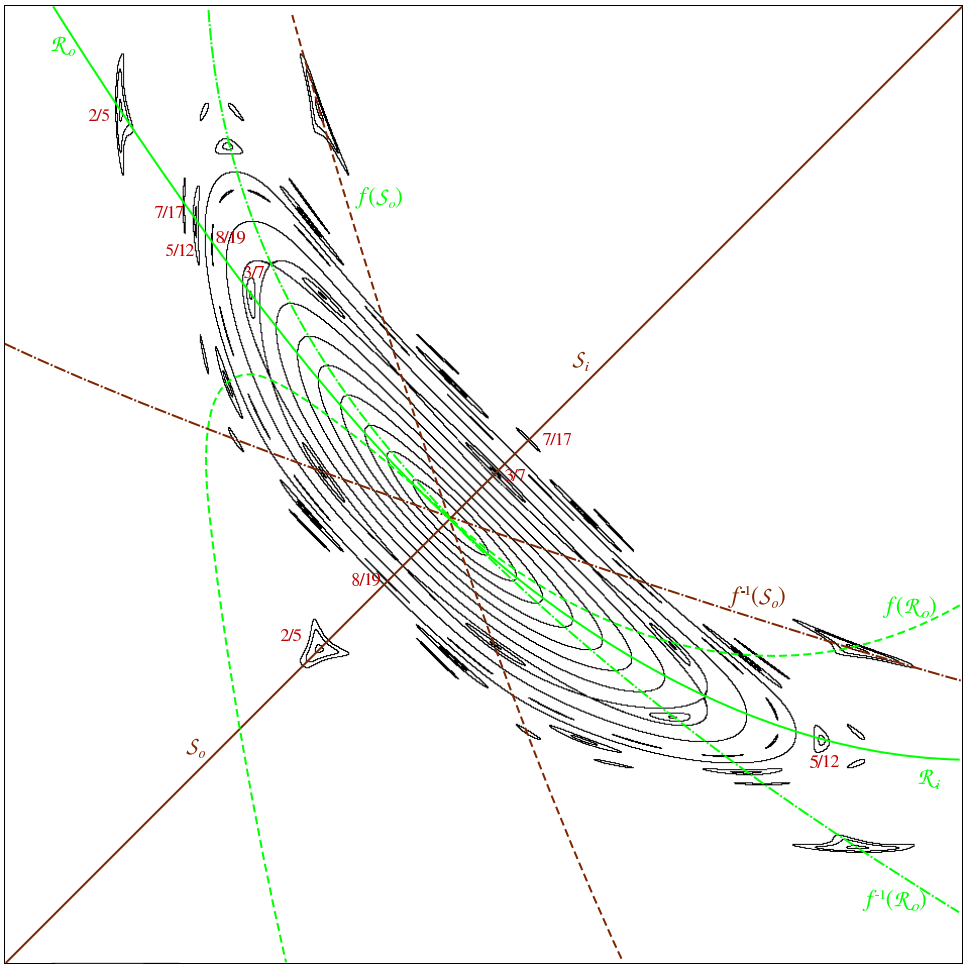

Figure 8: Phase space of the Hénon map for $k = 2.75$ with a range $(-1.75, 0)$ for x and x'. Shown are a number of orbits, including invariant circles around the elliptic fixed point, and five class-one island chains with rotation numbers $\frac{2}{5}, \frac{7}{17}, \frac{5}{12}, \frac{8}{19}, \frac{3}{7}$. Also shown are the four symmetry rays (solid curves) and their images (dashed curves) and preimages (dash-dot curves).

for maps similar to the standard map for large enough k [42]. For the Hénon map the dominant ray appears to be $\mathcal{R}_o$ for large values of k.

However, the identity of the dominant ray depends upon the monotonicity of the twist of the map. For the Hénon map, there is at least one anomalous domain, $\frac{9}{16} < k < \frac{5}{4}$, where the rotation number is increasing [31]. For orbits in an anomalous twist region, the elliptic and hyperbolic orbits reverse roles, and the ray $\mathcal{R}_o$ contains only hyperbolic orbits. As a result there is no dominant symmetry line that contains all elliptic orbits when the twist is reversed.

Under the assumption that $\mathcal{R}_o$ is dominant, we can easily determine which of the other symmetry rays contain points on the elliptic orbit, depending upon whether the numerator and/or the denominator of the rotation number are even or odd, see Table 2. The labeling of these lines is consistent with that in Fig. 8.

The time reversal symmetry operators also have a representation for the shift map, σ, Eq. (5). Indeed the interpretation of S is obvious if we consider its action on a configuration sequence: $S(x_{t-1}, x_t) = (x_t, x_{t-1})$. Thus as an operator on symbol sequences, S simply reflects them about

$\omega = \frac{p}{q}$	E_d	E_s	H_d	H_s
odd/odd	$\mathcal{R}_o$	$\mathcal{S}_i$	$\mathcal{R}_i$	$\mathcal{S}_o$
even/odd	$\mathcal{R}_o$	$\mathcal{S}_o$	$\mathcal{R}_i$	$\mathcal{S}_i$
odd/even	$\mathcal{R}_o$	$\mathcal{R}_i$	$\mathcal{S}_o$	$\mathcal{S}_i$

Table 2: The dominant(E_d, H_d) and subdominant(E_s, H_s) symmetry rays. Every elliptic (positive residue) class-one orbit (except when the twist is anomalous) is observed to have a point on E_d. Each row corresponds to rotation number $\frac{p}{q}$ with p and q even or odd as indicated.

the binary point

$$S(\ldots s_{-1}\boldsymbol{.}s_0 s_1 \ldots) = (\ldots s_1 s_0 \boldsymbol{.} s_{-1} \ldots)$$

For symbol sequences, it is convenient to use the operator $T = S\sigma$ for the second symmetry (instead of R), because this corresponds to a reflection about the symbol s_0:

$$T(\ldots s_{-1}\boldsymbol{.}s_0 s_1 \ldots) = (\ldots s_1 \boldsymbol{.} s_0 s_{-1} \ldots)$$

Thus the elements of the fixed set of S are sequences symmetric under a reflection about the binary point, and those of T are sequences symmetric under a reflection about s_0. Using the geometry of the horseshoe (see Appendix C) and its implied ordering relation given in Lemma 20, we can also find the codes for the symmetry rays. The o rays correspond to codes whose symbols are "smaller" than that for $(-)^\infty$. This means that the parity of sequence $s_0 s_1 \ldots s_j$, where s_j is the first symbol that is not $-$, must be negative, i.e., there must be an odd block of $-$ symbols after the binary point. Similarly the i rays correspond to codes that are "larger" than $(-)^\infty$, i.e. that have an even block of $-$'s (or none). More concretely, define $\kappa(\mathbf{s})$ to be the number of contiguous $-$ symbols following the binary point:[5]

$$\kappa(\mathbf{s}) = \min_{j\geq 0}\{j : s_j = +\} \tag{20}$$

then we have

$$\begin{aligned}
\mathcal{S}_o &= \{\mathbf{s} : s_{-t} = s_{t-1},\ \kappa(\mathbf{s}) \text{ odd}\}\ , \\
\mathcal{S}_i &= \{\mathbf{s} : s_{-t} = s_{t-1},\ \kappa(\mathbf{s}) \text{ even}\}\ , \\
\mathcal{T}_o &= \{\mathbf{s} : s_{-t} = s_t,\ \kappa(\mathbf{s}) \text{ odd}\}\ , \\
\mathcal{T}_i &= \{\mathbf{s} : s_{-t} = s_t,\ \kappa(\mathbf{s}) \text{ even}\}\ .
\end{aligned} \tag{21}$$

It is easy to see that the rotational codes of §3 are symmetric. For example, from Table 1, the code $\mathbf{s} = (\ldots{-}{-}{+}{+}{+}\boldsymbol{.}{-}{-}{+}{+}{+}\ldots)$ for the hyperbolic $\frac{1}{5}$ orbit has two points on symmetry lines, its first image $\sigma(\mathbf{s}) = (\ldots{+}{+}{+}{-}\boldsymbol{.}{-}{+}{+}{+}\ldots)$ is a point on $\mathcal{S}_o$ and $\sigma^3(\mathbf{s}) = (\ldots{-}{-}{+}\boldsymbol{.}{+}{+}{-}{-}\ldots)$ is a point on $\mathcal{T}_i$.

To prove this we start with a lemma about the symmetries of the rigid rotation Eq. (12). Though the reflection point for the rigid rotation is arbitrary, we choose $\theta = 0$, which conforms to the symmetry of our $W_\pm$ partitions, and to our selection of θ for the canonical elliptic code.

Lemma 3. *The rigid rotation $F(\theta) = \theta + \omega \mod 1$ can be factored as $F = ST$, with reversors $T : \theta \mapsto -\theta$, and $S : \theta \mapsto \omega - \theta$. When $\omega \leq \frac{1}{2}$, the fixed sets of these symmetries divide into the*

[5] $\kappa(\mathbf{s})$ does not exist for $(-)^\infty$, as it should not, since this point is the dividing point for the four rays.

rays

$$\begin{aligned} \mathcal{S}_o &= \{\theta : \theta = \tfrac{\omega}{2}\}\,, \quad \mathcal{S}_i = \{\theta : \theta = \frac{1+\omega}{2}\}\,, \\ \mathcal{T}_o &= \{\theta : \theta = 0\}\,, \quad \mathcal{T}_i = \{\theta : \theta = \frac{1}{2}\}\,. \end{aligned} \tag{22}$$

Points that start on these rays generate codes with symmetries given by Eq. (21).

Proof. Since the $W_\pm$ partition is symmetric with respect to $\theta = 0$, if we set $\theta_0 = 0$ then the resulting code is symmetric with respect to the binary point. Since $\theta_0 \in W_-$, and $\theta_1 = \omega \in W_+$, the sequence begins $\mathbf{.} - + \ldots$, so that $\kappa(\mathbf{s})$ is odd, agreeing with $\mathcal{T}_o$. Similarly, codes generated by $\theta_0 = \frac{1}{2}$ are also invariant under T, and start $\mathbf{.} + \ldots$, so they are on $\mathcal{T}_i$.

If we set $\theta_0 = \frac{\omega}{2}$, then the symmetry of the wedges (recall Fig. 4) implies $s_{-t} = s_{t-1}$, so the code is invariant under S. The first symbol is always $s_0 = -$; we will show that $\kappa(\mathbf{s})$ is odd. Indeed, when $\omega \leq \frac{2}{5}$, then $s_1 = +$, since $\theta_1 = \frac{3}{2}\omega \leq 1 - \omega$. Otherwise, $1 - \omega < \theta_1 < 1$, so that $s_1 = -$. But then $s_2 = -$ too, because $0 < \theta_2 < \omega$. Indeed, a double $-$ must occur whenever the orbit enters W_- having skipped W_+. Thus the line $\theta = \frac{\omega}{2}$ corresponds to $\kappa(\mathbf{s})$ odd, and is therefore $\mathcal{S}_o$. A similar argument gives the last case. □

Another simple lemma gives relations between the symmetry lines that imply the "dominant-subdominant" pairing in Table 2.

Lemma 4. *The four symmetry rays can be divided into two pairs (E_d, E_s) and (H_d, H_s), as given in Table 2 (depending on the parity of ω), such that if θ is a point on a dominant ray then $F^{\lceil \frac{q-1}{2} \rceil}\theta$ is a point on its subdominant partner. Moreover the iterates of lines from different pairs are disjoint.*

Proof. We consider only the case $\omega =$ odd/even; the others can be done similarly. First we prove that the stated pair of rays can be mapped into each other. That E_d is mapped into E_s is the statement $F^t(\mathcal{T}_o) = \mathcal{T}_i$ for some t. This requires that $t\omega = \frac{1}{2} + j$ for some integer j, which is equivalent to $\omega = \frac{2j+1}{2t}$. Thus ω is of the form odd/even, and $t = \frac{q}{2}$. For the $\mathcal{S}$ pair we similarly have $\frac{\omega}{2} + t\omega = \frac{1+\omega}{2} + j$, which again occurs when $t = \frac{q}{2}$. Since each pair maps to itself, it is enough to show that $\mathcal{T}_o$ does not map to $\mathcal{S}_o$, i.e. $F^t(\mathcal{T}_o) \neq \mathcal{S}_o$ for all t. This implies $t\omega \neq \frac{\omega}{2}$ mod 1. It is clear this equation does not have an integer solution for t for the odd/even case. Since $\mathcal{R}$ is the image of $\mathcal{T}$, this verifies the pairing in Table 2.

We find that for the odd q case $\mathcal{T}$ is mapped into $\mathcal{S}$ after $\frac{q+1}{2}$ iterations. Since we use $\mathcal{R}$ in Table 2, this decreases the number of iterates by 1. □

Finally, we use these results to show that the rotational codes have the symmetries as given in Table 2.

Theorem 5. *The codes for the rotational periodic orbits are symmetric. Moreover the canonically ordered elliptic code is on the dominant ray $\mathcal{T}_o$ (its image is on $\mathcal{R}_o$). The other symmetry lines occur as given in Table 2.*

Proof. The canonical code for an elliptic orbit has $\theta_t = \omega t$. Therefore, $\theta_0 = 0$, and Lemma 3 implies that this point is on $\mathcal{T}_o$. Since $f(\mathcal{T}_o) = \mathcal{R}_o$, the first image of the canonical code is on $\mathcal{R}_o$. Thus all elliptic orbits have points on the dominant symmetry line. By Lemma 4, they also must have a point on the subdominant line E_s.

The canonical code for the hyperbolic $\frac{p}{q}$ orbit has $\theta_t = \omega t - \frac{1}{2q}$ and the orbit covers the q evenly spaced points $\frac{2j-1}{2q}$, $j = 0, 1, \ldots q-1$ on the circle. Whenever p is odd, there exists a

time t' such that $2j-1=p$, and then $\theta_{t'}=\frac{p}{2q}=\frac{\omega}{2}$. Thus $\theta_{t'}\in\mathcal{S}_o$. If q is odd, then there exists a t'' such that $2j-1=q$ so that $\theta_{t''}=\frac{1}{2}\in\mathcal{T}_i$. This verifies the line H_d. The subdominant line then follows from Lemma 4. □

In particular, this implies that the dominant symmetry line conjecture follows from the rotational codes conjecture.

Corollary 6 (Dominant Symmetry Line). *If Conjecture 1 is true, then every elliptic class-one one parameter family of periodic orbits of the Hénon map starting at the AI limit until residue zero is encountered has a point on $\mathcal{R}_o$.*

The caveat in this corollary accounts for the domain of anomalous twist. The elliptic orbits born in this region in a rotational bifurcation have points on the H symmetry lines in Table 2, and connect to the normal-twist hyperbolic orbits in saddle-node bifurcations when they touch the twistless curve. Coming from the AI limit this saddle-node bifurcation is the first encounter of $r=0$, so the backwards running branch between $k(\omega)$ and $k_1(\omega)$ is removed, because there the statement is not true.

3.5 Symbol Boundary

According to Theorem 5, the boundaries of the wedges $W_\pm$ correspond to the image and preimage of a dominant symmetry line. Thus we expect that the symbol partition for class-one orbits will show this same structure. Indeed, this is what we observe, see Fig. 9. The figure shows that the wedge shaped symbol boundary leaving the elliptic fixed point (small magenta circle) is delineated by the image and preimage of $\mathcal{R}_o$, the dominant ray. This boundary also is valid for the nonrotational orbits shown.

An enlargement is shown in Fig. 10, where there is a prominent class-two island around the $\frac{2}{5}$ rotational orbit. Moving from the elliptic fixed point outward, the figure shows class-one periodic orbits with frequencies $\frac{16}{39}$, $\frac{9}{22}$, $\frac{20}{49}$, $\frac{11}{27}$, $\frac{13}{32}$, $\frac{15}{37}$, and $\frac{17}{42}$.[6] Notice that as expected from the schematic representation above, the $-$ region is a wedge with opening angle 2ω centered on the dominant symmetry line. Indeed as far as we can tell the symbol boundary for all rotational class-one orbits is indeed formed from the image and preimage of $\mathcal{R}_o$.

Also shown in Fig. 10 are three orbits that encircle the $\frac{2}{5}$ elliptic orbit—orbits of class two. To the resolution of this figure, it appears that the wedges formed from images of $\mathcal{R}_o$ also provide the symbol boundary for these orbits. However, as we will see in the sections below, this is not the case. We start by constructing the rotational codes for higher class orbits.

4 Class-Two Orbits

As first observed by Birkhoff, a typical elliptic periodic orbit has satellite periodic orbits in its neigbhorhood, i.e., orbits that rotate around the elliptic orbit. Some of these new orbits will in turn be elliptic and therefore have satellites about them as well. We use the term *class* to refer to this hierarchy of islands-around-islands [25]. For the Hénon map, the elliptic fixed point is defined to be class-zero, the rotational orbits of §3 are class one, and a class-two orbit is one that rotates around a class-one elliptic periodic orbit, see Fig. 8 for examples.

[6] It is convenient to use the Farey tree to choose periodic orbits. For $k=2.43$, the rotation number of the elliptic point is $\omega\approx 0.4123<\frac{7}{17}$. Starting with the pair of neighboring rationals $\frac{2}{5}$ and $\frac{7}{17}$, we construct the Farey tree for several levels to obtain our orbits.

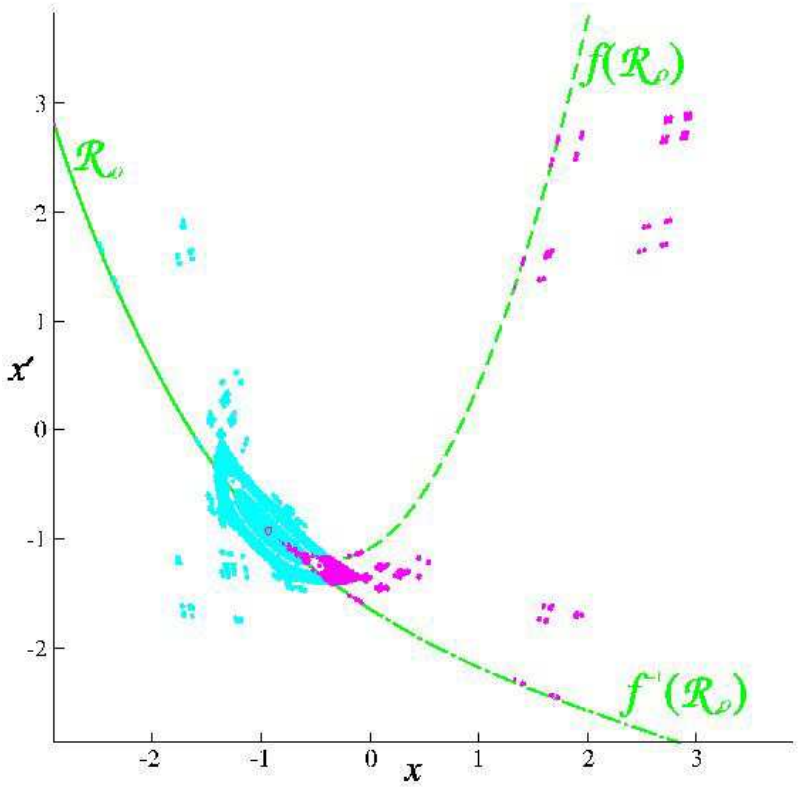

Figure 9: Symbol boundary for $k = 2.75$ appears to coincide with the image and preimage of the dominant symmetry line $\mathcal{R}_o$. Shown are the same orbits as in Fig. 3. Those points with $s_0 = +$ are colored magenta and those with $s_0 = -$ are cyan. The solid green line is the dominant symmetry line, $\mathcal{R}_o$, the dashed line is its image and the dot-dashed line its preimage.

Recall that an elliptic/hyperbolic pair of class-one periodic orbits with rotation number $\omega_1 = \frac{p_1}{q_1}$ is born at the elliptic fixed point when $k = k(\omega_1)$, Eq. (10). After its birth, the elliptic class-one orbit is the center of a class-two island chain consisting of the invariant circles and cantori that encircle each point on the class-one orbit. The island extends to the separatrix formed from stable and unstable manifolds of the class-one hyperbolic orbit, as schematically shown in Fig. 11. The class-two orbits have rotation numbers that are measured relative to f^{q_1}. When the linearized rotation number of the class-one orbit—as determined by its residue, Eq. (7) or Eq. (9)—passes through the rational frequency p_2/q_2, an elliptic/hyperbolic pair of class-two orbits is created in a q_2-tupling bifurcation of f^{q_1}. We denote the rotation number of these orbits by $\omega_1 : \omega_2$; they have period $Q = q_1 q_2$. Three such class-two orbits are shown in Fig. 10 with rotation numbers $\frac{2}{5} : \frac{1}{16}$, $\frac{2}{5} : \frac{1}{20}$ and $\frac{2}{5} : \frac{1}{22}$.

For the case of normal twist, the direction of rotation typically reverses with each increment of class. This occurs because in an any island the rotation number is typically a maximum at the elliptic orbit forming the island center and monotonically decreases to zero approaching the separatrix. In particular this implies that the inner separatrix of an island advances with respect to the center of the island and the outer one retreats, see Fig. 11. Continuity then implies that if the class-one invariant circles have clockwise dynamics, the class-two circles have

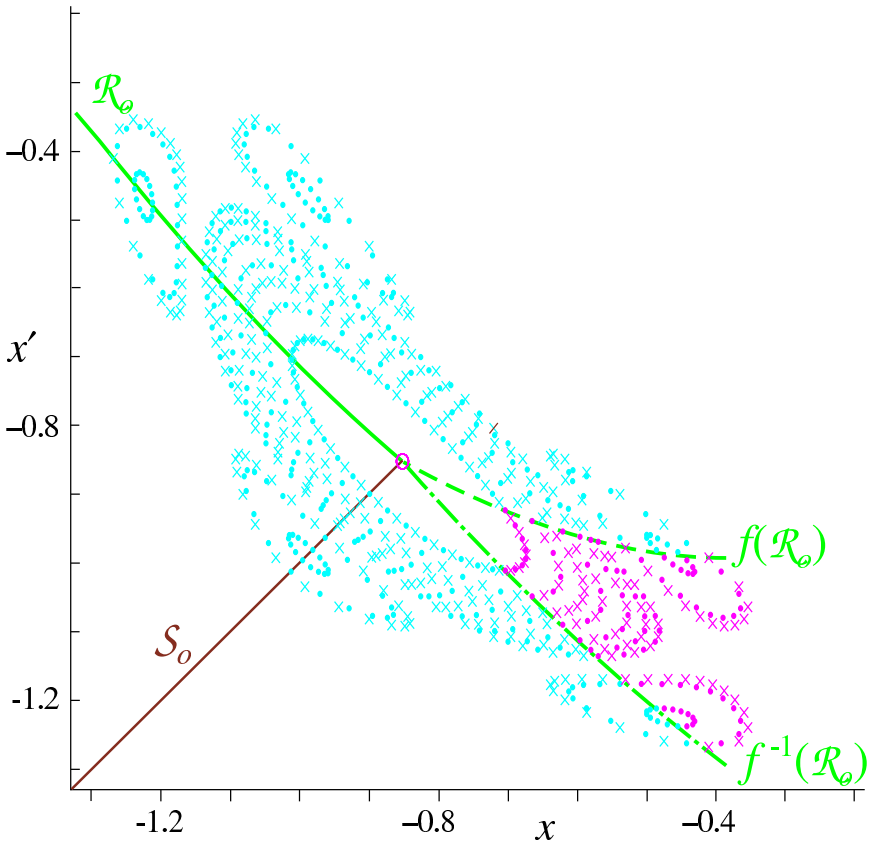

Figure 10: Class-one symbol boundary for $k \approx 2.43$ ($\epsilon = 0.54$) coincides with the image and preimage of the dominant symmetry line $\mathcal{R}_o$. Shown are 13 class-one rotational orbits about the elliptic fixed point, as well as three class-two orbits encircling the $\frac{2}{5}$ elliptic orbit. Elliptic (positive residue) orbits are shown as dots and hyperbolic as crosses.

counterclockwise dynamics.

Our numerical observations imply that the code for a class-two $\frac{p_1}{q_1} : \frac{p_2}{q_2}$ orbit is constructed essentially by repeating the class-one $\frac{p_1}{q_1}$ code q_2 times, because most of the class-two points are deeply buried inside the wedges shown in Fig. 4 that determine the class-one symbols. However, if the class-one sequence were merely repeated q_2 times, the orbit would not have the correct minimal period; consequently some of the symbols must be flipped to obtain the correct code. Indeed, there are two islands that intersect the class-one symbol boundary (recall the $\frac{2}{5}$ island in Fig. 10).[7] Such islands are termed *ambiguous* because they straddle the symbol boundary; the determination of the symbols of points in these special islands requires more analysis.

4.1 Class-Two Codes

Schematically, a class-one orbit with rotation number $\omega_1 = \frac{p_1}{q_1}$ can be represented as q_1 equally spaced points on a circle with the dynamics Eq. (12). In a similar vein, a class-two orbit with rotation number $\frac{p_1}{q_1} : \frac{p_2}{q_2}$ schematically corresponds to points on a set of circles enclosing each point of the class one orbit. To compute these points choose a pair of radii, r_1, r_2 to represent the sizes of the islands and define

$$x + iy = e^{-2\pi i\theta_1}\left(r_1 + r_2 e^{2\pi i\theta_2}\right) \ . \tag{23}$$

[7]Except for the case $\omega_1 = \frac{1}{2}$, where there is only one.

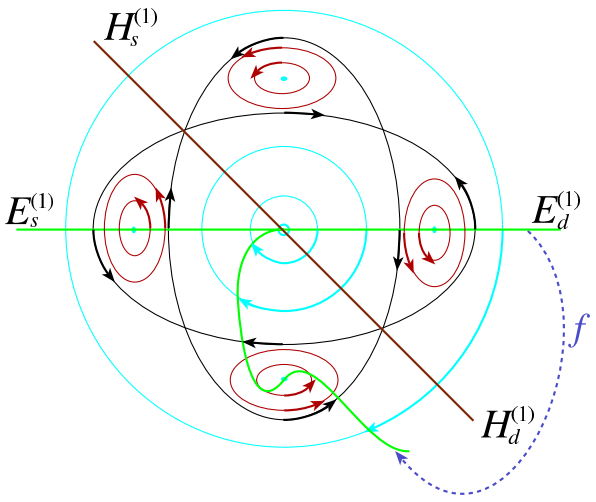

Figure 11: Schematic class hierarchy: class-one invariant circles (cyan) and a class-two $\frac{1}{4}$ island chain (red). Since the rotation number of the class-one circles decreases with radius, the image of the horizontal (green) line shears as shown. Continuity implies the direction of rotation reverses as the class is incremented. Also sketched are the elliptic (green) and hyperbolic (brown) symmetry rays for class-one.

Here r_2 chosen sufficiently smaller than r_1 so that none of the class-two islands intersect. This gives an *epicycle* view of the orbit. The angles (θ_1, θ_2), representing the island structure, evolve according to the two rotation numbers of the orbit. The schematic dynamics is expressed by using a mixed basis for time: $t = t_1 + q_1 t_2$ where $t_1 = t \mod q_1$ so that $t_i \in [0, q_i)$; this is written in clock-like notation as[8]

$$t \equiv t_1 : t_2 \, .$$

With this definition, the angles evolve as

$$\theta_i(t_i) = \omega_i t_i + \alpha_i \ , \ i = 1, 2 \, . \tag{24}$$

Iteration of this pair of maps produces a set of $Q = q_1 q_2$ points on the epicycle.

The signs in the exponentials in Eq. (23) are reversed to account for the reversal of rotation direction that occurs when moving between the classes.

Recall that the canonical elliptic class-one code is obtained by setting $\alpha_1 = 0$ and the hyperbolic code is obtained when $\alpha_1 = -1/2q_1$. Since class-two orbits rotate around elliptic class-one orbits, we set $\alpha_1 = 0$; the phase α_2 differentiates between the elliptic and hyperbolic class-two orbits. The canonical elliptic class-two code has $\alpha_2 = 0$, and the canonical hyperbolic code has $\alpha_2 = -\frac{1}{2q_2}$.

The epicycles for $\omega = \frac{2}{7} : \frac{2}{9}$ are shown in Fig. 12. The points of the elliptic class-one orbit are represented by filled circles evenly spaced along the large circle. Surrounding each of the q_1 points of this orbit is a smaller circle containing q_2 points of the class-two periodic orbit. By convention, we measure θ_2 in a corotating coordinate system, so that points with $\theta_2 = 0$ are

[8] Mixed base systems like the above are well known for time measurements, e.g. setting $\omega = \frac{1}{10} : \frac{1}{60} : \frac{1}{60} : \frac{1}{24} : \frac{1}{7} : \frac{1}{52}$ corresponding to tenth of seconds, seconds, minutes, hours, weekdays, weeks, so that in our notation $t = 0 : 1 : 30 : 19 : 4 : 5$ is the 4th day in the 5th week, at 19:30 hours plus 1.0 seconds. Instead of $\frac{1}{24}$ the American system uses $\frac{1}{12} : \frac{1}{2}$, where the 2 is represented as AM or PM. Our lives are simpler because all numerators are 1 for an actual clock, hence θ_j is not needed; they would have been even more so if the French revolution had succeeded in promulgating a decimal time system.

located on radial rays from the origin. Notice that a q_1-fold iteration maps each small circle to itself, shifting its points counterclockwise by ω_2.

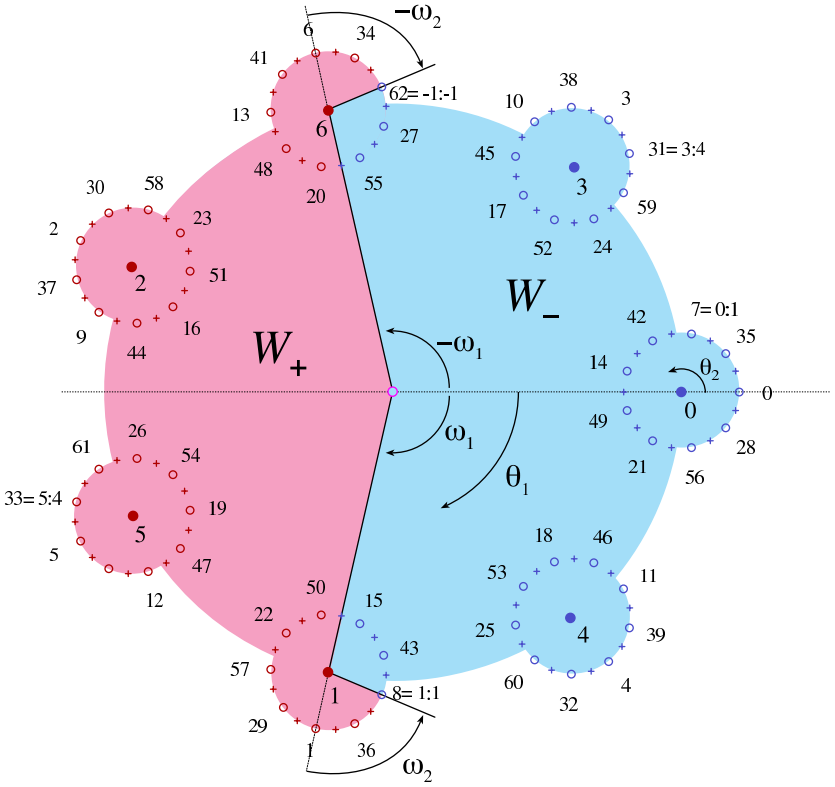

Figure 12: Epicycle view of a class-two orbit for $\omega = \frac{2}{7} : \frac{2}{9}$. The picture is generated by Eq. (23) with $r_1 = 1$ and $r_2 = 0.1$. The angle θ_1 is measured clockwise, and θ_2 counterclockwise. The elliptic class-one $\frac{2}{7}$ orbit is denoted with solid circles, and the class-two orbits are denoted by open circles (elliptic), and crosses (hyperbolic). Points with symbol $-$ are colored blue and those with $+$ are colored red. The integers next to each elliptic point denote the time t along the orbit.

To generate the symbol sequence for a class-two orbit, the epicycle picture must be partitioned into regions corresponding to the $+$ and $-$ symbols. Our observations indicate that this can be done by constructing a pair of "wedges" $W_\pm(\omega)$ whose boundaries are piecewise linear. The boundaries start as rays from the origin at angles $\theta_1 = \pm\omega_1$—these same rays formed the class-one boundary. The rays end in the center of the two ambiguous class-two islands corresponding to $t_1 = \pm 1$; it is not immediately clear how to continue the symbol boundary in these islands. A cursory look at Fig. 10 might indicate that the symbol boundary continues straight through the ambiguous islands. However, our numerical observations show that the two rays actually bend at the centers of the $t_1 = \pm 1$ ambiguous islands by angles $\theta_2 = \pm\omega_2$, respectively. This bending is too small to see in Fig. 10.

The regions $W_\pm(\omega_1 : \omega_2)$ bounded by these rays correspond to the $\pm$ symbols. Just as for the class-one case, the region containing $\theta_1 = 0$ corresponds to $s_t = -$. The only remaining point to understand is the symbol for points on the boundary. In contrast to class-one, our observations show that W_- is closed and W_+ is open.

Definition 2 (Class-Two Code). *$t = t_1 : t_2$ determines a point z in the plane by (23) and (24). If $z \in W_s(\omega_1 : \omega_2)$ then the tth symbol is s. The region $W_s(\omega_1 : \omega_2)$ is bounded by a continuous piecewise linear system of segments. At the origin two segments of length r_1 emerge*

at angles corresponding to $t_1 = \pm 1$. Their endpoints are connected to segments of length r_2 with angles corresponding to $t_1 : t_2 = \pm 1 : \pm 1$, see, e.g. Fig. 12. The region $W_-(\omega_1 : \omega_2)$ is the one that contains $t = 0 : 0$ and is closed, while $W_+(\omega_1 : \omega_2)$ is its complement.

It is not difficult to translate the epicycle picture into a simple algorithm that generates the codes for any $\omega = \frac{p_1}{q_1} : \frac{p_2}{q_2}$.

Continuing the example of Fig. 12, the orbits are coded so that the points in the red region have symbol + and those in the blue region have symbol −. The four points that fall on the symbol boundary (for example $t = 8 = 1 : 1$ and $t = 62 = 6 : 1$ for the elliptic orbit) have the symbol −. Note that points in the non-ambiguous islands, corresponding to $t_1 = 0, 2, 3, 4, 5$ have the same code as the elliptic class-one $\frac{2}{7}$ orbit. Thus many of the symbols of the class-two orbit simply repeat the class-one code.

To see this more clearly, denote the class one code by the row vector $\mathbf{s}_1$. Since most of the points on the class-two orbit are determined by this code, we first replicate this code q_c times; however, instead of viewing this as a vector of length $q_1 q_2$ we reshape the code as a table with $\mathbf{s}_1$ as its rows. The columns of this table are labeled by t_1, and the rows by t_2. In this way each ambiguous island corresponds to a column of the table, i.e. the columns $t_1 = 1$ and $t_1 = -1 \equiv q_1 - 1$. The codes in the ambiguous columns must now be replaced by the appropriate code for ω_2 using the class-two wedges.

As an example consider again the symbol sequence the $\frac{2}{7} : \frac{2}{9}$ orbit. The Table 3 lists the symbol sequence where the 63 symbols are arranged in 9 rows of 7 entries each. The ambiguous islands correspond to the columns $t_1 = 1$ and $t_1 = 6 = -1 \mod 7$. The $q_2(q_1 - 2)$ symbols in the remaining columns are determined by q_2-fold repetition of the elliptic class-one code for $\omega_1 = 2/7$, $(- + + - - + +)^\infty$.

t_1	0	1	2	3	4	5	6	t_2
	−	+	+	−	−	+	+	0
	−	**−**	+	−	−	+	+	1
	−	−	+	−	−	+	+	2
	−	+	+	−	−	+	−	3
	−	+	+	−	−	+	+	4
	−	+	+	−	−	+	+	5
	−	−	+	−	−	+	+	6
	−	**+**	+	−	−	+	−	7
	−	+	+	−	−	+	−	8

$\frac{2}{9}$	$\frac{2}{7} : \frac{2}{9}$	
s_t	$s_{1:t_2}$	$s_{-1:t_2}$
−	+	+
+	−	+
+	−	+
+	+	−
−	+	+
−	+	+
+	−	+
+	+	−
+	+	−

Table 3: Elliptic class-two code for the $\frac{2}{7} : \frac{2}{9}$ orbit. The ambiguous columns are $t_1 = 1$ and $t_1 = -1$. The hyperbolic code is the same with the exception of the boxed symbols, at $t = 8 = 1 : 1$ and $t = 50 = 1 : 7$, which are flipped. The right table compares the code for the elliptic $\frac{2}{9}$ class-one orbit with the two ambiguous columns in the $\frac{2}{7} : \frac{2}{9}$ orbit .

The symbols in the ambiguous columns $t_1 = \pm 1$ are generated with respect to a wedge formed by the boundary in the class-two island. The codes for the hyperbolic orbit are obtained by a shift of $\alpha_2 = -\frac{1}{2q_2}$, (i.e. a clockwise rotation) as shown in Fig. 12, this corresponds to flipping the two boxed symbols in Table 3. As we will see below, when there are two ambiguous

islands, exactly two symbols flip relative to the elliptic case.

Epicyclic pictures for additional class-two orbits are shown in Fig. 13. The codes are easily obtained from the figures by reading off the symbols according to the time t, using the colors shown. For example, the code for the elliptic $\frac{1}{9} : \frac{3}{7}$ orbit is the 7 fold repetition of the $\frac{1}{9}$ elliptic code, $-+^8$, modifying only two symbols in the columns $t_1 = \pm 1$, by setting $s_{10} = s_{62} = -$. The hyperbolic code is obtained from the elliptic one by flipping s_{10} to $+$, and s_{55} to $-$.

As ω_1 approaches $\frac{1}{2}$, the class-one $+$ wedge shrinks to a single point $\theta_1 = \frac{1}{2}$. Orbits with $\omega_1 = \frac{1}{2}$ are special because the two boundaries of the class-one wedge coincide so that there is only one ambiguous island with $t_1 = +1 \equiv -1$. Thus for example, the code for the $\frac{1}{2} : \frac{1}{8}$ elliptic orbit shown in the last panel of Fig. 13 is $(- + -^{14})^\infty$, while its hyperbolic partner has code $(- + -^{13}+)^\infty$. In this case the ambiguous column of the elliptic orbit contains $+-^7$ while the unambiguous column simply contains $-^8$.

If ω_2 approaches $\frac{1}{2}$, as in the first two panels of Fig. 13, the open class-two wedges grow encompassing all but $\theta_2 = \frac{1}{2}$. The extreme case of this, $\omega_2 = \frac{1}{2}$ has only one $s = -$ point in the ambiguous islands; for example, the code for the elliptic $\frac{1}{8} : \frac{1}{2}$ orbit is $(- +^7 - - +^5 -)^\infty$.

The well-known "doubling" substitution rule

$$- \to - + \text{ and } + \to - - \tag{25}$$

(see Appendix B) can be used to generate the codes for class-two orbits of the form $\frac{1}{2} : \omega$ from those of the class-one orbit with frequency ω. For example, applying this substitution rule to the $\frac{1}{8}$ code, $-+^7$, gives the same code as in Fig. 13. That this is true in general follows because the class-two wedge for $s = +$ is $\theta_2 \in (-\omega, \omega)$, which is the same as the class-one wedge for $s = -$. Hence each symbol flips to create the ambiguous column; the first, unambiguous column is all $-$.

4.2 Numerical Observations

In this section we present numerical observations that support the class-two code construction for the area-preserving Hénon map. As for the class-one case in §3.3, we checked that the class-two orbits defined by their codes at the AI limit collide with the appropriate class-one orbit at the parameter value where the class-one orbit has the expected residue. We restricted our attention to class-two orbits with q_1 and $q_2 \leq 13$. Fig. 14 shows the number of digits of precision in the bifurcation value for the class-two rotational orbits with normal twist.[9] When $\omega_1 = 1/2$ there is only a single ambiguous class-two island. In order to verify the class-two code for this case we compared the numerical bifurcation parameters for 236 class-two orbits of the form $\frac{1}{2} : \omega_2$ where $q_2 < 39$ to the exact value [40]

$$k(\frac{1}{2} : \omega_2) = 3 + \sin(\pi\omega_2)^2 \, .$$

Outside of the interval below $\omega_2 = 1/3$ where the twist vanishes at class-two the computed values of the bifurcation parameter were accurate (to at least 8 significant digits) when compared to the exact value.

The results we have obtained give us confidence to formulate the following

Conjecture 2. *The AI code for the class-two orbits of the Hénon map is defined by the wedges $W_\pm(\omega_1 : \omega_2)$ given in §4.1.*

[9] There are only eight orbits with fewer than four digits of precision: $\frac{1}{3} : \frac{4}{13}, \frac{1}{4} : \frac{4}{13}, \frac{1}{5} : \frac{4}{13}, \frac{2}{5} : \frac{4}{13}, \frac{2}{7} : \frac{4}{13}, \frac{5}{12} : \frac{3}{13}, \frac{5}{13} : \frac{4}{13}, \frac{6}{13} : \frac{6}{13}$. These are probably related to anomalous twist either near $\frac{1}{3}$ or near $\frac{1}{4}$.

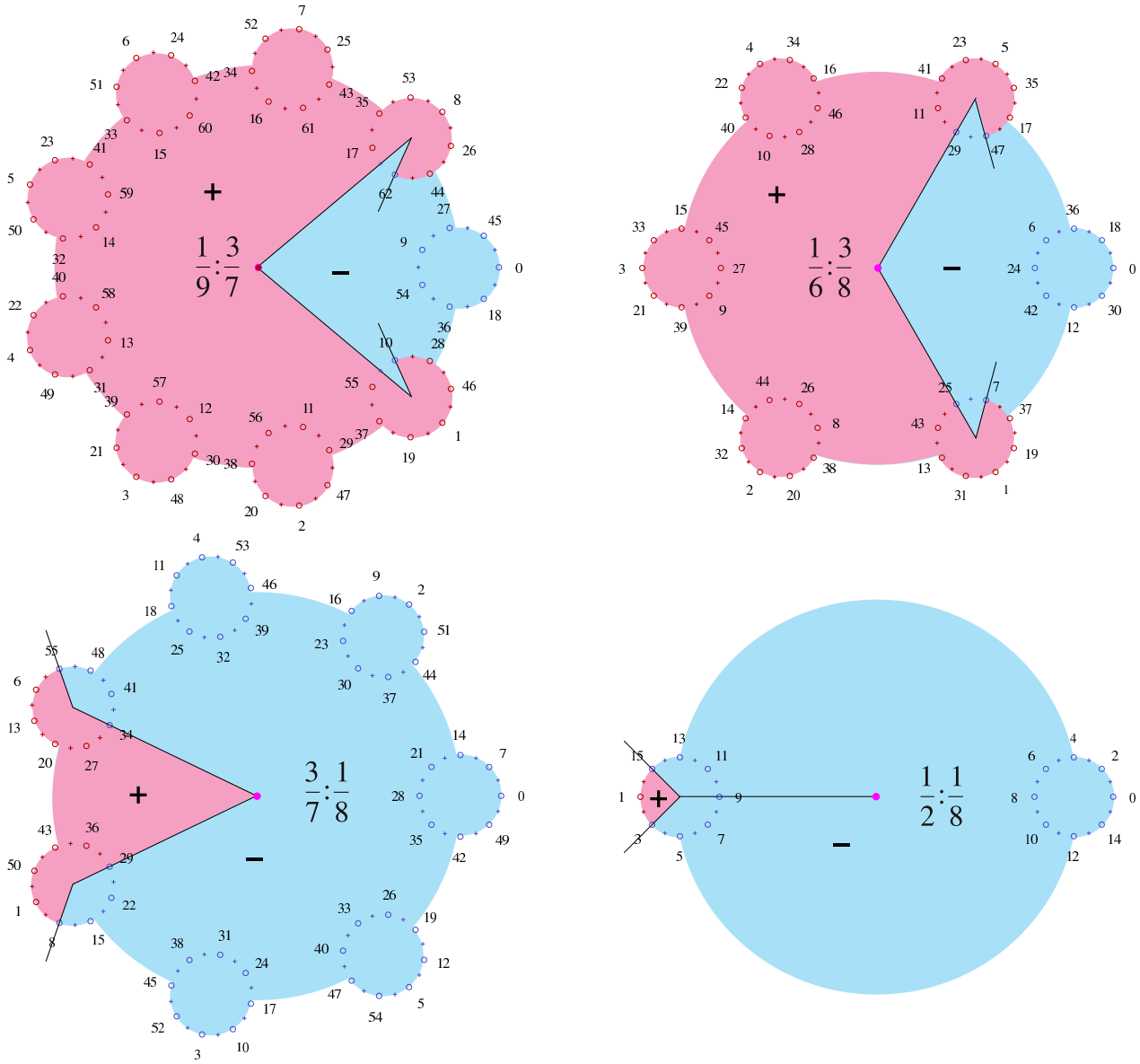

Figure 13: Four examples of schematic class-two orbits. Points are labeled by the time t along the orbit. Symbols in the blue regions are $-$ and in the red regions are $+$.

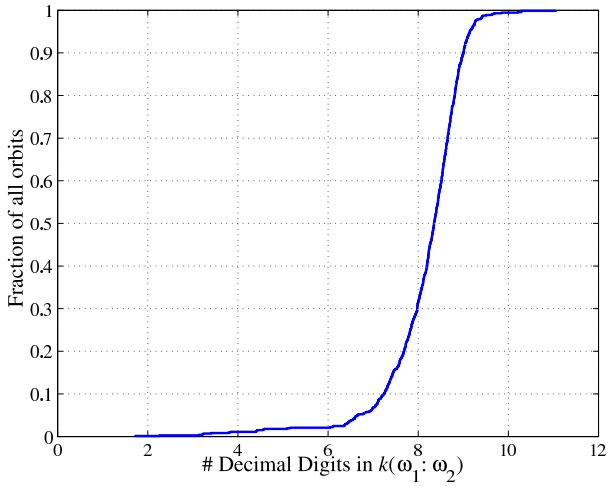

Figure 14: Number of correct digits in parameter value for 727 class-two orbits with $q_1 \leq 13$ and $q_2 \leq 13$. We excluded frequencies $p_2/q_2 = 1/3, 3/10$ where the class-one twist is anomalous to avoid numerical difficulties with multiple bifurcations.

4.3 Parity of Class-Two Codes

We now show that the elliptic and hyperbolic class-two codes differ by two symbols, but they have the same parity.

Lemma 7 (Properties of class-2 codes). *Assume $\omega \neq \frac{1}{2} : \frac{1}{2}$. Then the elliptic and hyperbolic class-2 codes differ by flipping two symbols, the symbol at $t = 1 : 1$ and that at*

$$t = -1 : \frac{q_2}{2} \qquad q_2 \text{ even}$$
$$t = 1 : \frac{q_2(2j+1)+1}{2p_2} \qquad q_2 \text{ odd}$$

where j is the smallest non-negative integer for which an integer solution for t_2 is obtained. The parity of both orbits is equal to the parity of q_2.

Proof. We start by considering the ambiguous island, $t_1 = +1$. By definition, the hyperbolic and elliptic codes differ only when $\omega_2 t_2$ and $\omega_2 t_2 - \frac{1}{2q_2}$ are in different wedges. Let S_j be the sectors defined in Eq. (15) relative to q_2 for θ_2. When q_2 is *even* the situation is similar to class-one, because the the wedge boundaries in the ambiguous island coincide with boundaries of some sectors S_j. Accordingly only the symbol $t = 1 : 1$ changes. Alternatively when q_2 is *odd*, the other wedge boundary at $\frac{1}{2}$ is not part of the elliptic orbit since $\omega_2 t_2 \not\equiv \frac{1}{2}$ for all t_2. Instead the hyperbolic orbit hits this boundary when $\omega_2 t_2 - \frac{1}{2q_2} = \frac{1}{2} + j$, flipping the symbol at this location. This gives the above formula. In order to show that this is the only other change with $t = 1 : t_2$ the argument of Lemma 1 can be repeated with sectors $\tilde{S}_j$ of half the size. As a result for all $\alpha_2 \in \tilde{S}_{-1}$ the elliptic code is obtained, while for $\alpha_2 \in \tilde{S}_{-2}$ the hyperbolic code is obtained.

Now we consider the ambiguous island with $t = -1 : t_2$. The wedge in this island is a reflection of that in the previous ambiguous island. However, since the rotation direction is not reversed, the sectors S_j (or $\tilde{S}_j$) are not reflected. This implies that whenever an open sector end coincides with a closed wedge end for $t = +1 : t_2$, after reflection of the wedge for $t = -1 : t_2$ both endpoints will be open, and vice versa. Since a symbol flip only occurs when different types

of endpoints coincide only one of the symbols at $t_2 = \pm 1$ flips, never both. In particular when q_2 is *odd* both symbol flips occur for $t_2 = +1$, while for *even* q_2 the symbol half way around the orbit with $\omega_2 t_2 = \frac{1}{2} + j$ flips for $t_2 = -1$. This gives the first part of the lemma.

When q_2 is even the parity of the unambiguous symbols ($t_1 \neq \pm 1$) is even, because their number per island is multiplied by q_2. The parity of the ambiguous symbols is even in the elliptic case, because the symbol sequences are cyclic permutations of each other: Starting with $\alpha_2 = 0$ at $t_1 = 1:1$ gives the same symbol sequence as starting with $\tilde{\alpha}_2 = \frac{1}{2} - \omega_2$ at $t = -1 : \frac{q_2}{2}$ (apply a rotation!). But $\tilde{\alpha}_2$ is a point on the orbit for even q_2, hence the elliptic ambiguous columns have the same numbers of signs. Therefore their parity is even, and the whole sequence has even parity when q_2 is even.

When q_2 is odd the parity of the unambiguous symbols is odd, because the number per island is odd and they are repeated an odd number of times. The number per island is odd because the elliptic class-one orbits have odd parity, and the two deleted symbols in the ambiguous column are + signs in the elliptic case. The number of signs in the ambiguous columns is the same because the two are time reversals of each other: upon reflection of the wedge and the orientation the same sequences are generated. So their parity is even, and the total parity is odd. □

Recall from Lemma 2 that the elliptic/hyperbolic class-one orbits have opposite parities and this corresponds to their opposite residue signs. One important consequence of the previous lemma is that at class two the elliptic/hyperbolic partners have the same parity and therefore, according to Eq. (8), will have residues with the same sign at the AI limit. Nevertheless they are initially born with opposite residues, as this is the normal form of the q_2-tupling bifurcation [34]. According to Eq. (8) even parity implies a negative residue at the AI limit. Therefore, when q_2 is even the residue of the (initially) elliptic orbit, which is (initially) positive, must cross $r = 0$ at least once as k increases from the bifurcation value in the approach to the AI limit. Similarly, when q_2 is odd the residue of the (initially) hyperbolic orbit must cross $r = 0$ for some k larger than the bifurcation value.

We call bifurcations related to these additional zeros in the residue function *secondary bifurcations*. In particular when $r = 0$ for k larger than the parameter value of the rotational bifurcation, a secondary pitchfork bifurcation occurs (super- or subcritical, depending on the parity of the code), and when $r = 1$ a secondary period-doubling bifurcation occurs (again super- or subcritical, depending on the parity). Between these two parameter values, a complete sequence of secondary rotational bifurcations must take place. An example of these bifurcations is shown in Fig. 15.

We will not attempt to completely describe the symbol sequences associated with these secondary bifurcations, but only offer an empirical rule based on our numerical observations:

Conjecture 3 (Pitchfork class-two). *The pitchfork children of class-two orbits only differ in the four symbols at the intersection of the ambiguous columns and rows with t_1 and t_2 given in Lemma 7. When q_2 is* even *these four symbols ordered by t are $-+--$ for the (initially) elliptic orbit and $++-+$ for the (initially) hyperbolic orbit. The secondary bifurcation of the elliptic orbit is*

$$-+-- \to \mathrm{pf}(-+-+, -++-)\,.$$

When q_2 is odd *they are $-++-$ for the elliptic and $++--$ for the hyperbolic orbit. The secondary bifurcation of the hyperbolic orbit is*

$$++-- \to \mathrm{pf}(+++-, ++-+)\,.$$

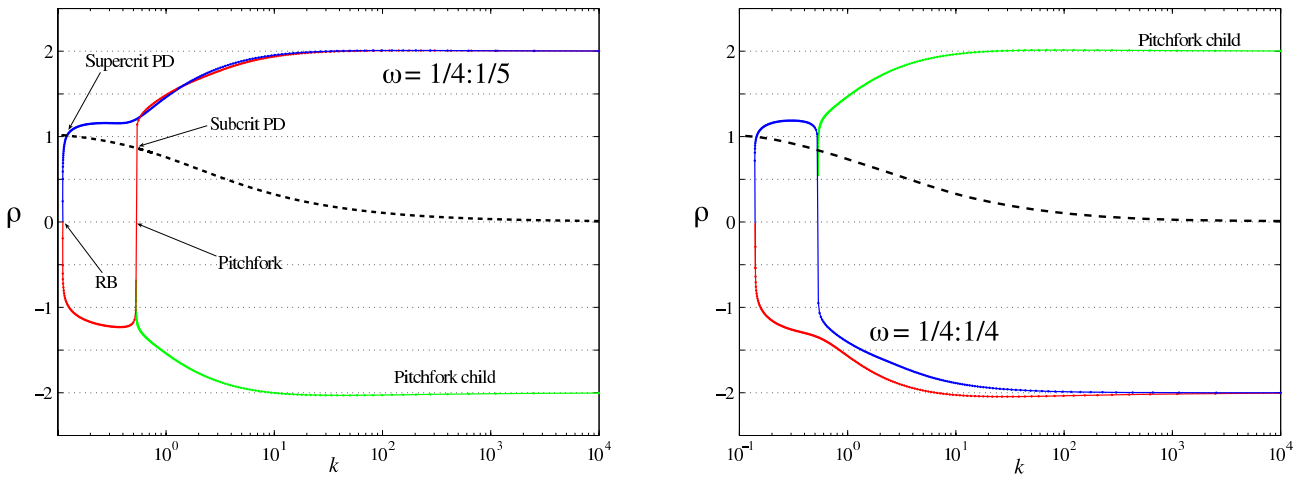

Figure 15: Scaled residue ρ, Eq. (11), for typical class-two rotational orbits and their pitchfork children with q_2 odd (left panel) and even (right panel). The (initially) stable class-two orbit is rendered in blue, the (initially) unstable orbit in red, and one of pitchfork children in green. The dashed curve is the period-doubling curve $r = 1$. The secondary pitchfork bifurcation occurs at the rightmost zero crossing on the (initially) stable orbit when q_2 is even and the initially unstable orbits when q_2 is odd.

It is not hard to show that the four ambiguous symbols in the parent sequence must be $\mp + --$ as given in Conjecture 3; these are the symbols corresponding to the points on the appropriate class-two wedge boundaries.

The rule given in Conjecture 3 generates the symbol sequences of the daughter orbits created in a secondary pitchfork bifurcation. These are the orbits whose residues are rendered in green in Fig. 15. We examined 105 class-two orbits in the Hénon map with frequencies of the form $\frac{1}{j} : \frac{p}{q}$ where $j = 3, 4, 5$ and $3 \le q \le 15$. The parameter value (k) where the pitchfork children predicted by Conjecture 3 were born agreed (to at least eight significant figures[10]) with the value where the residue of the class-two parent orbit crossed zero in the "secondary" bifurcation. These results suggest that the conjecture is probably valid for the Hénon map.

4.4 Symmetries

Numerical observations suggest that the concept of "dominant" symmetry line can be extended to class-2 orbits (and in fact to class-c with $c > 2$, see below); for example, for each ω_1, there appears to be a particular symmetry ray that contains all of the elliptic class-two orbits $\omega_1 : \omega_2$ [25]. Recall from Table 2 that there are two rays, E_d and E_s, whose identity depends upon the parity of the numerator and denominator in ω_1, that contain elliptic class-one orbits. Since each class-two orbit rotates around the points on a class-one orbit, they should have points on the two E rays. These two rays are divided at the class-one elliptic points, giving four new rays. As before, we use i and o to denote "inward" and "outward" halves of the rays; the subscript i corresponds to the ray that starts at the elliptic class-c orbit and heads in toward the elliptic class-$(c-1)$ orbit, while o is the ray that heads out from the lower class orbit. Thus, for example, E_s is divided into E_{so} and E_{si}. We denote the four symmetry rays at class-c by $E_d^{(c)}, E_s^{(c)}, H_d^{(c)}$,

[10] With the exception of a six orbits: $\frac{1}{3} : \frac{4}{13}, \frac{1}{4} : \frac{4}{11}, \frac{1}{4} : \frac{4}{13}, \frac{1}{4} : \frac{5}{13}, \frac{1}{4} : \frac{5}{14}, \frac{1}{5} : \frac{4}{13}$ for which numerical difficulties gave less than six digits of precision.

and $H_s^{(c)}$. The observation in [25] is that

$$E_d^{(c)} = E_{so}^{(c-1)}\,; \tag{26}$$

that is, the outward half of the class-$(c-1)$ subdominant ray becomes the dominant ray for class-c, see Fig. 16. This is consistent with Fig. 10, as all of the elliptic, class-two $\frac{2}{5} : \frac{p_2}{q_2}$ orbits have a point on the outward half of $E_s^{(1)} = \mathcal{S}_o$.

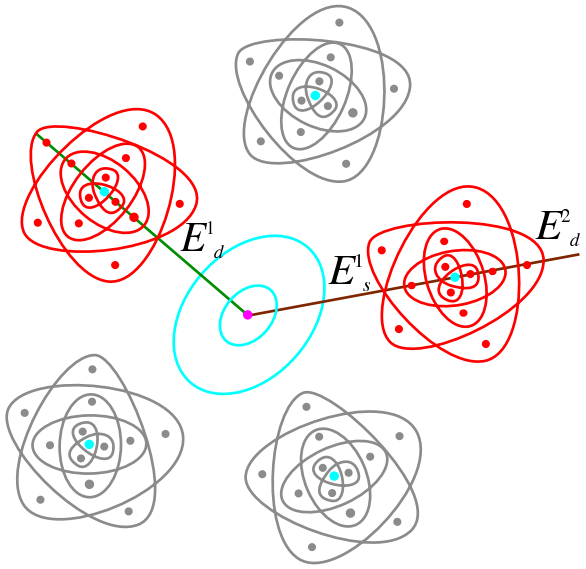

Figure 16: Sketch of the dominant symmetry line at class-two. Shown are points on a period 5 elliptic class-one orbit (cyan dots), and several class-two orbits (red on the symmetric islands) All of the elliptic class-two orbits line up on the outward half of the subdominant class-one ray $E_{so}^{(1)}$.

In this section we verify the dominant symmetry conjecture for the class-two codes. We also obtain a recipe to describe the boundary of the class-two wedge in terms of iterates of the $E_d^{(2)}$, so that the wedge can be computed in the Hénon map and compared to the prediction obtained from numerical continuation.

That the class-two elliptic codes are symmetric is a simple consequence of the symmetry of the wedges $W_\pm$ in the two epicycle picture.

Lemma 8 (Symmetries of class-two codes). *Let* $\mathbf{s}$ *be the code for the elliptic class-two orbit with rotation number* $\omega = \frac{p_1}{q_1} : \frac{p_2}{q_2}$. *Then* $\mathbf{s}$ *has an image on the dominant symmetry line* $E_d^{(2)} = E_s^{(1)}$. *In addition, when* q_2 *is odd,* $\mathbf{s}$ *has an image on the subdominant line* $E_s^{(2)} = E_d^{(1)} = \mathcal{R}_o$, *and when* q_2 *is even on* $E_s^{(1)}$. *Here* $E_{d,s}^{(1)}$ *are the lines in Table 2.*

Proof. Let $\mathbf{s}$ denote the canonical elliptic symbol sequence, i.e. starting from the point $\theta = (0, 0)$. Then if $t_+ = 1 : 1 = 1 + q_1$, the point $\sigma^{t_+}\mathbf{s}$ is on the symbol boundary since it corresponds to $\theta = (\omega_1, \omega_2)$. Similarly setting $t_- = -1 : -1 \equiv (q_1 - 1) : (q_2 - 1) = q_1 q_2 - 1 \equiv -1$, then $\sigma^{t_-}\mathbf{s}$ is also on the symbol boundary, and corresponds to $\theta = (-\omega_1, -\omega_2)$. Since the class-two wedge W_- is closed, these two points have the same first symbols $s_0 = -$, and by symmetry of the wedges in $\theta \mapsto -\theta$, the two sequences must be the same when reversed; consequently,

$$T\sigma^{t_+}\mathbf{s} = \sigma^{t_-}\mathbf{s}\,.$$

Repeatedly composing this with σ, and noting that $\sigma T = T\sigma^{-1}$, we find that when $t_+ + t_-$ is even, $\sigma^a \mathbf{s} \in \mathcal{T}$ where $a = \frac{t_+ + t_-}{2} = \frac{q_1}{2}$. Alternatively when $t_+ + t_-$ is odd, since $\sigma T = S$ we find $\sigma^b \mathbf{s} \in \mathcal{S}$ where $b = \frac{t_+ + t_- + 1}{2} = \frac{q_1+1}{2}$.

To decide which half of the symmetry line these points are on, recall from Eq. (20) that this is determined by $\kappa(\mathbf{s})$, the number of consecutive $-$ symbols starting at s_0. Consider first q_1 even, where the symmetric point is $\sigma^a \mathbf{s}$. Since $t = a = \frac{q_1}{2} : 0$, then $\theta = (\frac{\omega_1 q_1}{2}, 0) = (\frac{p_1}{2}, 0) = (\frac{1}{2}, 0)$ because p_1 is necessarily odd. Thus the first symbol of this sequence is $s_0 = +$, and so by Eq. (22) it is on $\mathcal{T}_i$. When q_1 is odd, the symmetric point is $\sigma^b \mathbf{s}$, with $t = \frac{q_1+1}{2} : 0$, and so $\theta = (\frac{p_1}{2} + \frac{\omega_1}{2}, 0)$. When p_1 is even, this is on the line $\theta_1 = \frac{\omega_1}{2}$, with $s_0 = -$; following the argument in Lemma 3 this implies the point belongs to $\mathcal{S}_o$. Similarly when p_1 is odd, the point is in $\mathcal{S}_i$.

Summarizing we obtain the table:

ω_1	$t_1{:}t_2$	θ_1	θ_2	$E_d^{(2)}$
odd/odd	$\frac{q_1+1}{2}{:}0$	$\frac{1}{2} + \frac{\omega_1}{2}$	0	$\mathcal{S}_i$
even/odd	$\frac{q_1+1}{2}{:}0$	$\frac{\omega_1}{2}$	0	$\mathcal{S}_o$
odd/even	$\frac{q_1}{2}{:}0$	$\frac{1}{2}$	0	$\mathcal{T}_i$

Since this symmetry is independent of ω_2, we are justified in calling it a "dominant" symmetry line.

The subdominant symmetry line can by found by noting that since $\mathbf{s}$ has period $Q = q_1 q_2$, we also have

$$T\sigma^{t_+}\mathbf{s} = \sigma^{t_- + Q}\mathbf{s}$$

Iterating this relation we find that if $q_1(q_2+1)$ is even, then $\sigma^c \mathbf{s} \in \mathcal{T}$ when $c = \frac{t_+ + t_- + Q}{2} = \frac{q_1(q_2+1)}{2}$. Otherwise, $\sigma^d \mathbf{s} \in \mathcal{S}$ where $d = \frac{q_1(q_2+1)+1}{2}$.

The choice of ray for the subdominant symmetry depends upon the parity of both ω_1 and ω_2. When q_2 is odd, then the second line is at $\sigma^c \mathbf{s}$. Indeed $t = c = 0 : \frac{q_2+1}{2}$, and so $\theta_1 = 0$ independently of ω_1, and $\theta_2 = \frac{p_2}{2} + \frac{\omega_2}{2}$. For any p_2 we have $\sigma^c \mathbf{s} = \mathbf{.} - + \ldots$, so that this point is on $\mathcal{T}_o$.

We now consider q_2 even. If q_1 is also even then the symmetry still occurs at $t = c = \frac{q_1}{2} : \frac{q_2}{2}$, which gives $\theta = (\frac{p_1}{2}, \frac{p_2}{2}) = (\frac{1}{2}, \frac{1}{2})$ since both p's are odd. If $\omega_1 < \frac{1}{2}$, then $s_o = +$, and the symmetry is $\mathcal{T}_i$. A similar argument gives the same result for the frequency $\frac{1}{2}$ case. The final case has q_1 odd and q_2 even, for which the symmetry corresponds to $t = d = \frac{q_1+1}{2} : \frac{q_2}{2}$, so that $\theta = (\frac{p_1}{2} + \frac{\omega_1}{2}, \frac{p_2}{2})$. When p_1 is even, $\theta_1 = \frac{\omega_1}{2}$, so $s_0 = -$. This point is on $\mathcal{S}_o$, as follows from an argument similar to that in Lemma 3. Finally if p_1 is even $\kappa(\mathbf{s})$ is even, so the symmetry is $\mathcal{S}_i$.

Summarizing, we obtain a table for the subdominant line:

ω_1	ω_2	$t_1{:}t_2$	θ_1	θ_2	$E_s^{(2)}$
any	even/odd	$0{:}\frac{q_2+1}{2}$	0	$\frac{\omega_2}{2}$	$\mathcal{T}_o$
any	odd/odd	$0{:}\frac{q_2+1}{2}$	0	$\frac{1}{2} + \frac{\omega_2}{2}$	$\mathcal{T}_o$
odd/odd	odd/even	$\frac{q_1+1}{2}{:}\frac{q_2}{2}$	$\frac{1}{2} + \frac{\omega_1}{2}$	$\frac{1}{2}$	$\mathcal{S}_i$
even/odd	odd/even	$\frac{q_1+1}{2}{:}\frac{q_2}{2}$	$\frac{\omega_1}{2}$	$\frac{1}{2}$	$\mathcal{S}_o$
odd/even	odd/even	$\frac{q_1}{2}{:}\frac{q_2}{2}$	$\frac{1}{2}$	$\frac{1}{2}$	$\mathcal{T}_i$

□

So far we have shown that the class-two codes are consistent with Eq. (26), but we have not yet shown how to divide $E^{(1)}$ into halves.

Theorem 9 (Class 2 Dominant Symmetry Ray). *The dominant symmetry ray for class-two codes is the outward half of the subdominant ray at class-one, $E_d^{(2)} = E_{so}^{(1)}$, thus verifying Eq. (26) for class-two.*

Proof. The division of the symmetry lines for the shift σ into rays at the class-one orbit uses the ordering relation discussed in Appendix C. As shown in Fig. 23, the outer halves of $\mathcal{S}_o$ and $\mathcal{T}_o$ correspond to codes that are "less" than (under this special ordering) those of the class-one orbit, while the outer halves of $\mathcal{S}_i$ and $\mathcal{T}_i$ correspond to codes that are "greater" than those of the class-one orbit. The canonical elliptic class-two code is the same as that of the class-one orbit up to time $t = 1 : 1 = 1 + q_1$, where it first hits the class-two wedge boundary. Moreover, according to Lemma 8 and Lemma 4, if $\mathbf{s}$ is the canonical elliptic code, then its $\lfloor \frac{q_1+1}{2} \rfloor$th iterate is on $E_s^{(1)}$

Thus the relative ordering of the class-one and class-two codes, following Lemma 20, depends upon the parity of the symbols of the class-one orbit starting halfway around the orbit, and going up to the first differing symbol $s_{q_1+1} = s_1$, i.e. on the sign of

$$\rho = \pi(s_{\lfloor \frac{q_1+1}{2} \rfloor} \dots s_{q_1-1} s_0 s_1) \ ,$$

In particular, we must show that $\rho = (-1)^{p_1}$. This follows because if p_1 is even, $E_s^{(1)} = \mathcal{S}_o$, and so the code for the class-one orbit should be greater than that of the class-two orbit, while if p_1 is odd, then the symmetry lines are either $\mathcal{S}_i$ and $\mathcal{R}_i$, so the class-one code should be less than that for class-two.

As noted in Lemma 2, the class-one elliptic code has $2p_1 - 1$ symbols that are $-$. Moreover, the canonical elliptic code has symmetry T, which means it is unchanged under reflection about $s_0 = -$. This implies that the first half of the orbit $s_1 s_2 \dots s_{\lfloor \frac{q_1-1}{2} \rfloor}$ is the same as the second half $s_{\lfloor \frac{q_1+1}{2} \rfloor} \dots s_{q_1-1}$ written backward. Consequently they each have $p_1 - 1$ symbols that are $-$. Finally, the sequence $s_{\lfloor \frac{q_1+1}{2} \rfloor} \dots s_{q_1-1} s_0 s_1$ has one additional minus sign, making p_1 in total; therefore, $\rho = (-1)^{p_1}$. □

4.5 Symbol Boundary

In order to connect the above findings to the Hénon map we now describe the wedge boundaries in terms of iterates of symmetry lines. Inside the class-one island the wedge boundary is simply given by the forward and backward iterate of the dominant symmetry ray $\mathcal{R}_o$, as discussed in §3.5. From the schematic picture it would seem as if the higher class wedges are also constructed from iterates of $\mathcal{R}_o$. This would, however, contradict the observation that the dominant symmetry line is different at the next class [25]. Moreover, we expect that a symbol boundary should be associated with a line containing all the elliptic points. Thus, as we saw in Lemma 8 it should be associated with the subdominant elliptic line.

Therefore we now show that appropriate iterates of $\mathcal{R}_o$ in the schematic picture can in fact be identified with certain iterates of the subdominant lines as given by Eq. (26).

Lemma 10 (Boundary Symmetry Lines). *The boundaries of the class-two wedge in the ambiguous islands $t_1 = \pm 1$ for the class-two orbit $\omega = p_1/q_1 : p_2/q_2$ are given by*

- *the $\lfloor \frac{q_1-1}{2} \rfloor + t_1$ iterate of the subdominant symmetry ray $E_s^{(1)}$ and*
- *the $-\lceil \frac{q_1+1}{2} \rceil$ iterate of symmetry ray $E_{do}^{(1)}$.*

Proof. Recall the proof of Lemma 4. The schematic boundary of the class-two wedge has two parts. The inner part consists of the class-one rays $F^{t_1}(\mathcal{R}_o)$ with $t_1 = \pm 1$. The first part of the lemma is the statement that this ray is an image of $E_s^{(1)} = \mathcal{S}_o$. For example, when $\omega_1 = e/o$, then we require that there exists an integer n such that

$$\omega_1 = \frac{even}{odd}: \quad F^{t_1}(\mathcal{R}_o) = F^n(\mathcal{S}_o) \quad \Rightarrow \quad \omega_1(t_1+1) + j = \frac{\omega_1}{2} + \omega_1 n$$

for some integer j. Solving for ω_1 gives $2j/(2n - 2t_1 - 1)$, which is of the form $even/odd$. When $t_1 = 1$ the explicit solution is $n = (q_1 + 3)/2$, and when $t_1 = -1$ it is $n = (q_1 - 1)/2$. Note that replacing $\mathcal{S}_o$ by $\mathcal{S}_i$ or $\mathcal{R}_i$ leads to a contradiction. Hence $\mathcal{S}_o$ is the unique symmetry ray that can be mapped to $\mathcal{R}_o$ for $\omega_1 = even/odd$. In a similar way the other cases lead to

$$\omega_1 = \frac{odd}{odd}: \quad F^{t_1}(\mathcal{R}_o) = F^n(\mathcal{S}_i) \quad \Rightarrow \quad \omega_1(t_1+1) + j = \frac{1+\omega_1}{2} + \omega_1 n$$

which gives the same values of n as before. Finally,

$$\omega_1 = \frac{odd}{even}: \quad F^{t_1}(\mathcal{R}_o) = F^n(\mathcal{R}_i) \quad \Rightarrow \quad \omega_1(t_1+1) + j = \frac{1}{2} + \omega_1(n+1)$$

which gives $n = \frac{q_1}{2} + t_1$. Combining theses expressions gives the first form.

The second ray of the class-two wedge is formed by taking the o part of the ray just constructed (i.e. the part that goes beyond radius r_1), and turning it by $\pm\omega_2$ for $t = \pm 1$, respectively. Turning by $\pm\omega_2$ is achieved by iterating one complete cycle of class-one, i.e. iterating $\pm q_1$ times. For $t_1 = -1$ the number of iterates is thus $(q_1 - 1)/2 - q_1$ for odd q_1 and $q_1/2 - 1 - q_1$ for even q_1. Combining both cases gives $-\lceil (q_1+1)/2 \rceil$, and the result follows. □

As a result of the previous Lemma the number of iterates needed to construct the class-two wedge only depends on q_1, the period of the class-one orbit.

It seems pointless to construct the class-two wedge from iterates of the new dominant symmetry line instead of from iterates of $\mathcal{R}_o$, since the two agree in the schematic picture. It turns out, however, that the former gives the correct wedges for the Hénon map. In the schematic pictures the two constructions coincide because the map has no twist. At the birth of the class-two island (when the rotation number of the class-one orbit is ω_2, and the rotation number of the class-two orbit is 0) the schematic picture is an accurate description of the wedge-geometry. Away from this bifurcation the symbol boundary differs from that in the schematic picture, and the wedge needs to be constructed from the dominant lines of class 2.

In Fig. 17, we show the symbol boundary for $k = 2.684$, where the $\frac{2}{5}$ island is predominant (the same phase space is shown in Fig. 18). Here the class-one orbits are shown with colors cyan and magenta for $s = \pm$, respectively. The boundary between these colors is given by the image and preimage of $\mathcal{R}_o$ as before. Class-two orbits with $\omega = \frac{2}{5} : \frac{p_2}{q_2}$ are shown with colors blue and red for $s = \pm$. Note that the class-one partition boundary does not work for these orbits. According to Lemma 4 the boundaries in the $t_1 = -1$ ambiguous island are given by segments of $f^2(\mathcal{S}_o)$ and $f^{-3}(\mathcal{S}_o)$; these are shown as the dashed (brown) curves, and clearly delineate the symbol boundary in Fig. 17 for the class-two orbits. Similarly segments of $f^4(\mathcal{S}_o)$ and $f^{-1}(\mathcal{S}_o)$ form the class-two boundary in the $t_1 = 1$ ambiguous island.

There is apparently a jump in the symbol boundary across the separatrix of the $\frac{2}{5}$ orbit. We are unable to resolve the behavior near the separatrix numerically as the period of the orbits near the separatrix becomes too large to accurately find the bifurcation values numerically.

The ability to describe the wedge boundary that is obtained by continuation from the AI limit in terms of iterates of the symmetry lead to Conjecture 2.

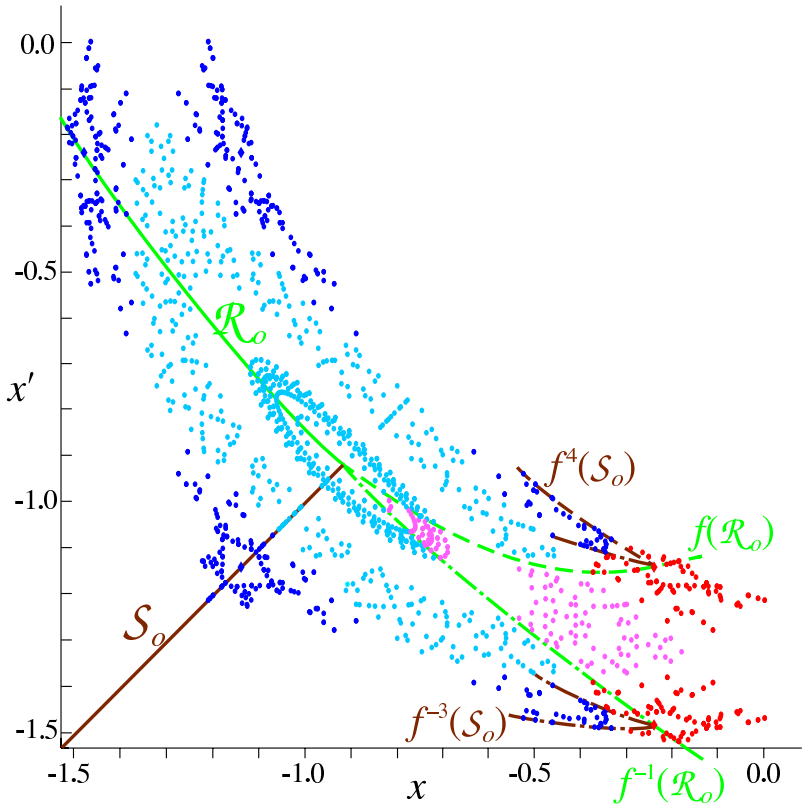

Figure 17: Class-one (cyan and magenta) and class-two (blue and red) rotational orbits for $k = 2.684$. The $-$ symbols correspond to the cyan and blue points, and the $+$ to magenta and red. Also shown are the $t = \pm 1$ iterates of the symmetry line $\mathcal{R}_o$ (green) that form the class-one boundary, and the iterates $t = -1, 4$ and $t = -3, 2$ of $\mathcal{S}_o$ (brown) that form the class-two boundary.

5 Class-c Codes

Orbits of arbitrarily high classes can also be found in area-preserving maps. For example, Fig. 18 shows successive enlargements of the phase space of the Hénon map and exhibits orbits up to class four. The enlargements in this figure are not done with the same multiplier; indeed, though there are special parameter values for which the class hierarchy exhibits self-similarity [25], in general it does not. While there are typically islands of every class, their shape and structure changes with class.

A class-c orbit rotates around a class-$(c-1)$ elliptic periodic orbit with some definite rotation number. We denote the rotation number by a string

$$\omega = \omega_1 : \omega_2 : \ldots : \omega_c \; . \tag{27}$$

Each of the numbers $\omega_i = \frac{p_i}{q_i}$ is necessarily rational, except possibly ω_c. If the class-c orbit is periodic, it has period $Q = \prod_{i=1}^{c} q_i$. The rotation number ω_{c+1} about a class-c periodic orbit is obtained by iterating f^Q and considering rotations about one point on the class-c orbit—if an orbit returns to itself after q_{c+1} iterations of f^Q and has undergone p_{c+1} full rotations, then $\omega_{c+1} = \frac{p_{c+1}}{q_{c+1}}$.

Generalizing the epicycle picture in Fig. 12, we can construct the symbol sequences for periodic orbits of arbitrary class. As before, time is written in the mixed q_i basis:

$$t = t_1 + q_1 \left(t_2 + q_2 \left(t_3 + \ldots + q_{c-1} t_c \right) \right) \equiv t_1 : t_2 : \ldots : t_c \, ; \tag{28}$$

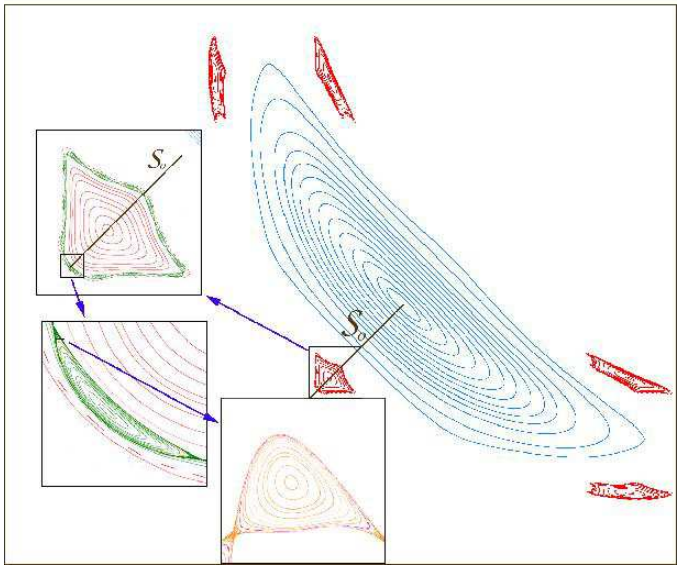

Figure 18: Phase space of the Hénon map for $k = 2.684$. Enlargements show higher class orbits, ultimately focusing on the $\frac{2}{5} : \frac{3}{13} : \frac{1}{18} : \frac{1}{17}$ orbit. The class-one invariant circles (cyan) encircle the elliptic fixed point, class-two (red) the $\frac{2}{5}$ elliptic orbit (red). Shown in the enlargements are class-three circles (green), class-four (orange), and finally a class-five chain (mauve). The elliptic class-two $\frac{2}{5} : \frac{3}{13}$ orbit has a point on the subdominant elliptic line $\mathcal{S}_o$ for the elliptic $\frac{2}{5}$ orbit, as implied by dominant symmetry line conjecture.

where the digits t_i are taken modulo q_i. Associated with each t there is a point $\theta(t) \in \mathbb{T}^c$ defined by the mapping

$$t \mapsto \theta(t) = (\omega_1 t_1, \omega_2 t_2, \ldots, \omega_c t_c + \alpha_c) \ . \tag{29}$$

Here we have set $\alpha_j = 0$ for $j = 1, 2, \ldots c-1$; this represents the selection of elliptic orbits up through class-$(c-1)$. The phase α_c selects an elliptic or hyperbolic class-c orbit. A class-j island consists of the set of points $\theta(t)$ with a fixed choice of $t_1 : t_2 : \ldots : t_{j-1}$. Incrementing t_j moves the orbit around the island with frequency ω_j, while incrementing θ_j by $\frac{1}{q_j}$ moves sequentially through the points in the island.

The epicycle picture is obtained by generalizing Eq. (23). Define a set of radii, r_i, $i = 1, \ldots c$, that decrease rapidly enough so that the set of circles defined by

$$x + iy = e^{-2\pi i \theta_1} \left(r_1 + e^{2\pi i \theta_2} \left(r_2 + \ldots r_c e^{(-1)^c 2\pi i \theta_c} \right) \right) \ , \tag{30}$$

do not overlap. As before, the direction of rotation reverses with each class. An example epicycle picture for class three is shown in Fig. 19.

The definition of the class-c code is complete once we specify the boundary between the "wedges" $W_\pm$ that define the symbols $s_t = \pm$. As for class-two, our numerical observations indicate that the boundary consists of another wedge. The rays that bound the wedge leave the origin with angles $\theta_1 = \pm\omega_1$. These extend to the center of the two class-two ambiguous islands at $t_1 = \pm 1$. The rays turn by angles $\theta_2 = \pm\omega_2$, and continue to the center of two class-three ambiguous islands at $t = 1 : 1$ and $t = -1 : -1$, respectively. The rays again turn by angles $\theta_3 = \pm\omega_3$, continuing to the center of class-four ambiguous islands, etc. Note that since the direction of rotation in Eq. (30) reverses, the rays turn in an alternating manner.

The specification of the symbol boundary is complete once we define the codes for points that fall on the boundary. This is especially important for $c > 2$, as there can be more than

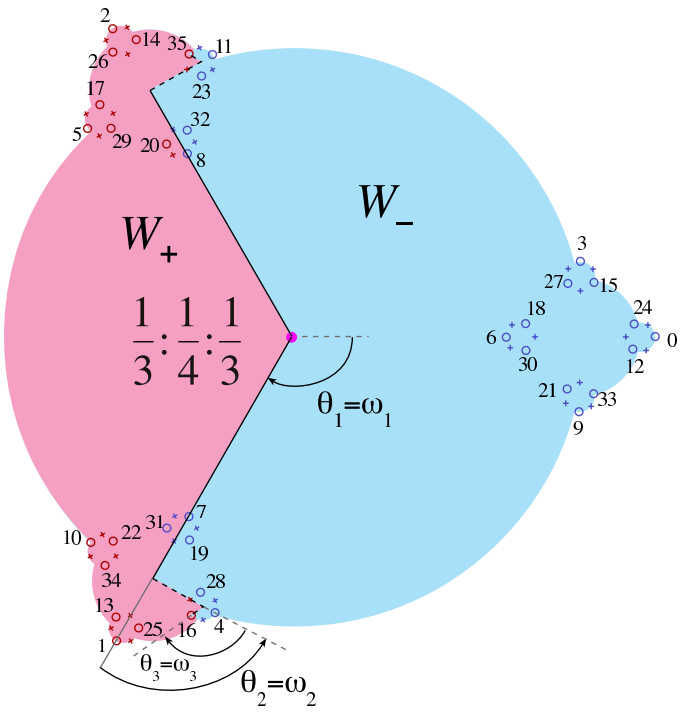

Figure 19: Epicycle picture for the class-three orbit $\frac{1}{3} : \frac{1}{4} : \frac{1}{3}$. The boundary of W_- (blue) is closed on the solid rays and open on the dashed rays.

two ambiguous islands. For example in Fig. 19, since $q_2 = 4$ is even, there are four ambiguous class-two islands, corresponding to $t = 4 = 1 : 1$, $7 = 1 : 2$, $8 = -1 : -2$ and $11 = -1 : -1$—and the rays defining the boundary of W_- intersect all of these islands. By contrast, when q_2 is odd, there are only two ambiguous class-two islands, $t = 1 : 1$ and $-1 : -1$.

The openness/closedness state of the boundary of the region W_- is most easily described recursively. Recall that at class one, the boundary of W_- is open. Given the boundary at class $(c-1)$, the boundary at class c is obtained by reversing the state of the ray at class $c-1$ and appending class-c rays with the same state. Thus for class-two, the previously open class-one ray becomes closed, and the new class-two ray is also closed. For class three, as shown in Fig. 19, the class-two ray and the new class-three ray are now open. Applying this rule to the first few classes generates Table 4.

class	r_1	r_2	r_3	r_4	r_5
1	- - -				
2	—	—			
3	—	- - -	- - -		
4	—	- - -	—	—	
5	—	- - -	—	- - -	- - -

Table 4: The class-c boundary of W_- is open (dashed) or closed (solid) along the rays, r_c, defining the ambiguous islands.

We have checked that this rule works for a number of class-three orbits, and a few orbits

of class four. However, the high periods and multiplicity of secondary bifurcations involved prohibit systematic studies of high class orbits. In particular for the class-two orbit $\frac{1}{3} : \frac{1}{4}$, this rule generates the correct codes for the elliptic and hyperbolic orbits with $\omega_3 = \frac{1}{2}$, $\frac{1}{3}$, $\frac{1}{4}$, $\frac{1}{5}$, and $\frac{2}{5}$. We have also checked the case $\frac{1}{4} : \frac{1}{4} : \frac{1}{3}$ and a number of cases with odd q_2 including $\frac{1}{3} : \frac{1}{3} : \frac{1}{4}$. The correct code is also obtained for $\frac{1}{3} : \frac{1}{4} : \frac{1}{2} : \frac{1}{2}$. The class-$c$ codes also work for the period doubling case where it is equivalent to the doubling substitution rule, recall Eq. (25). For example, the codes for the period-doubling sequence through class four are

$$\begin{array}{ll} \frac{1}{2} : \frac{1}{2} & (-+--)^\infty \\ \frac{1}{2} : \frac{1}{2} : \frac{1}{2} & (-+---+-+)^\infty \\ \frac{1}{2} : \frac{1}{2} : \frac{1}{2} : \frac{1}{2} & (-+---+-+-+---+--)^\infty \end{array} \tag{31}$$

A simple rule that also generates this sequence is to double the previous entry and flip the last symbol [40].

Though we have not systematically explored beyond class-two, these few studies give us confidence that the class-c rule works in general.

6 Conclusion

We have shown how to systematically generate symbolic codes for rotational orbits and "islands-around-islands" orbits for the area-preserving quadratic map. The construction of the codes in terms of wedges with opening angles determined by the frequencies ω_c of the orbits explains numerical observations of the wedge-shaped symbol boundaries for elliptic islands. The wedge boundaries are constructed from segments of the symmetry lines of the mapping.

It is for precisely this case—when there are elliptic orbits—that more traditional, symbolic partitions fail. It is interesting to note that Christiansen and Politi constructed symbol boundaries in islands of the standard map that have precisely the same structure as ours for class-one rotational orbits [21]. However, for this case the identification of symmetry lines is complicated by the fact that the standard map has two distinct sets of reversors.

Open questions that we hope will be investigated in the future include:

- How does the symbol boundary evolve from the line $x = 0$ when there is a horseshoe, to the complex set of epicycle-generated wedges when there are elliptic islands? Note that when an orbit first becomes stable, it typically does so by an inverse period-doubling, so its wedge opening angle will be zero.

- Does the epicycle picture for rotational codes also apply to other reversible, area-preserving maps with anti-integrable limits? Examples include the standard mapping, and polynomial automorphisms.

- How do the wedge boundaries connect across the island separatrices? As was first observed in [21], the symmetry lines seem to naturally connect with the symbol boundary in the chaotic region of phase space that corresponds to primary tangencies. They remark: "We have no explanation for this nice phenomenon." Neither do we.

- What are the codes for rotational orbits generated by bifurcations of the elliptic orbits created in secondary pitchfork and twistless bifurcations?

- How are the symbol boundaries organized in maps that are not reversible? Perhaps the simplest example corresponds to some quartic polynomial automorphisms [43]?

A Codes for Twist Maps

Our purpose in this appendix is to relate the rotational codes described in this paper to those used in other papers. There are three commonly used codes for rotational orbits of twist maps, the linear, velocity and acceleration codes, which we denote a, b, and c respectively [24, 44, 45, 46].

Aubry-Mather theory implies that recurrent minimizing orbits for twist maps have a particularly simple symbolic coding. Orbits that are nondegenerate minima of the action are hyperbolic. Thus the codes we discuss here will correspond to the hyperbolic codes in §3.

An area-preserving map on the cylinder $f : \mathbb{S}^1 \times \mathbb{R}$

$$(x', y') = f(x, y) \tag{32}$$

is a monotone twist map if $\frac{\partial x'}{\partial y} > 0$. Note that this hypothesis does not apply to the Hénon map, even locally about $(-)^\infty$, because it has a twistless bifurcation at $k = \frac{9}{16}$ leading to a twist reversal [31]. Nevertheless, we will see that the c-codes for minimizing orbits of twist maps do correspond to those of the rotational Hénon map with the proper translation.

A.1 Linear Code

One way of coding rotational orbits of maps with an angle variable is to count the number of complete rotations they make. To do this, we lift the angle variable to the line, and define the linear code,

$$a_t = \lceil x_t \rceil \ .$$

Thus a_t is the number of complete rotations at time t.[11]

The linear code of a minimizing orbit of a twist map is determined by its rotation number.

Theorem 11 (Aubry [37]). *Suppose $F : \mathbb{R}^2 \to \mathbb{R}^2$ is a lift of the twist map Eq. (32), and $\{x_t, t \in \mathbb{Z}\}$ is the configuration of a recurrent, minimizing orbit. Then there exists a rotation number ω and phase α such that the linear code of x_t is the same as that for the rigid rotation on the circle $\theta_t = \omega t + \theta_0$, i.e.,*

$$a_t = \lceil \omega t + \alpha \rceil \tag{33}$$

Here we take Eq. (33) as the definition of the linear code for a rotational orbit and consider some simple structures that arise.

A.2 Velocity Code

An alternative coding for rotational orbits is the "velocity" code, defined to be the first difference of the a-code:

$$b_t \equiv a_{t+1} - a_t \tag{34}$$

Note that knowledge of **b** gives **a** up to an initial condition, a_0, which corresponds to the choice of interval for the lifted angle x_0.

While, the b-code is well defined for any ω, if we restrict to $0 \le \omega < 1$ then we can compute it by dividing the circumference-one circle into two sectors

$$\begin{aligned} B_1(\omega) &\equiv (-\omega, 0] \ , \\ B_0(\omega) &\equiv (0, 1-\omega] \ . \end{aligned} \tag{35}$$

[11] The choice of the ceiling function here is arbitrary, as are the choices of forward and backward finite differences in the next two sections. Ultimately, these only affect the canonical ordering for the codes, but the ordering is important for concatenation rules.

Then we have

$$b_t = i \quad \text{if} \quad \{\omega t + \alpha\} \in B_i(\omega) \,, \tag{36}$$

as shown in Fig. 20.

When ω is irrational, the code changes as α varies. We define the "canonical" ordering as that obtained by setting $\alpha = 0$. For example the canonical b-code for γ^{-2} is

$$\mathbf{b} = (\ldots 0100.10100101001001010010100100101001001010010\ldots) \,.$$

The fact that there are uncountably many hyperbolic codes is consistent with the fact that there are uncountably many orbits on a particular invariant circle or cantorus. Note that the velocity code always consists of blocks of the form (10^m) and (10^{m-1}) where $m = \lfloor \omega^{-1} \rfloor$. As we will see below, it is no accident that these building blocks are the codes for the Farey parents $\frac{1}{m+1}$ and $\frac{1}{m}$ of each frequency in the interval that they bound.

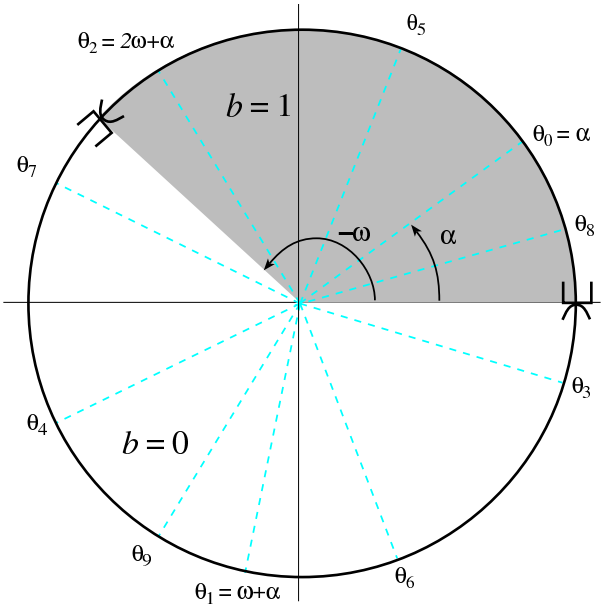

Figure 20: Construction of the velocity code for $\omega = \gamma^{-2}$ showing the sectors B_0 and B_1 (shaded). The orbit shown has $\alpha = -0.1$ and its b-code is $(\ldots 0100.1010010010\ldots)$.

When $\omega = p/q$ is rational the velocity code is independent of choice of initial phase.

Lemma 12. *The b-code for a rational rotation number $\omega = p/q$ is independent of the choice of phase α up to cyclic permutations.*

Proof. The S_j defined in Eq. (15) partition the circle into q sectors of width $\frac{1}{q}$. Note that $B_0 = \bigcup_{j=0}^{q-p-1} S_j$, and $B_1 = \bigcup_{j=q-p}^{q-1} S_j$ so the b-code is determined by these sectors. Since for any α the points $\theta_t = \{\omega t + \alpha\}$ are spaced uniformly on the circle at a distance $\frac{1}{q}$ from each other, there is precisely one θ_j in each S_j. Thus the number of 0 and 1 symbols is independent of α. Moreover if $\theta_t \in S_j$, then $\theta_{t+1} \in S_{j+p}$, so that the cyclic order of symbols is independent of α. □

Note in particular, that all values $-1/q < \alpha \leq 0$ give the canonical velocity code. Other values of α, give a cyclic permutation of this "canonical" ordering for the code.

Corollary 13. *For $\omega = p/q$ the b-code has p 1's and $q - p$ 0's.*

The velocity codes for various frequencies can be easily constructed using a Farey tree procedure [23, 3]. A Farey tree is a binary tree that generates all numbers in an interval between two "neighboring" rationals [47]. A pair of rationals $\frac{p}{q} < \frac{m}{n}$ are neighbors if

$$mq - pn = 1$$

The Farey tree is recursively constructed beginning with a base defined by a neighboring pair, and recursively applying the Farey sum operation

$$\frac{p}{q} \oplus \frac{m}{n} \equiv \frac{p+m}{q+n} \ ,$$

to each neighboring pair. Note that $\frac{p}{q} < \frac{p}{q} \oplus \frac{m}{n} < \frac{m}{n}$, and that the daughter is a neighbor to each of its parents.

For example, the two rationals $\frac{0}{1}$ and $\frac{1}{1}$ define the base for a Farey tree that includes all numbers in the unit interval, see Fig. 21. The root of the tree, or level zero, is the daughter rational defined by the Farey sum of the base rationals. In this case the root is $\frac{1}{2}$. Each subsequent level of the tree consists of the rationals that are the Farey sum of each number on the previous level with its two neighbors at earlier levels, thus there are 2^j rationals at level j.

Every irrational $\omega \in [0, 1]$ is uniquely determined by a path defined by an infinite sequence of left, L, and right, R, transitions beginning at the root of the Farey tree. Every rational $\omega \in [0, 1]$ is uniquely determined by a finite path. For example, the path for $5/13$ is $LRLR$. There are also paths in the Farey tree that do not correspond to real numbers: for example $LRLLLLLLL\ldots$ limits to $\frac{1}{3}$, but is better thought of as $\frac{1}{3_+}$. Dynamically this sequence corresponds to a homoclinic orbit. The paths of the parents of any rational are easy to obtain by appropriately truncating its path; for example, given a path $LRLLL = \frac{5}{14}$, then the direct parent is obtained by simply removing the last symbol, $LRLL = \frac{4}{11}$. The other parent is obtained by removing all of the final repeated symbols (L in this case) in the sequence and one more symbol, yielding the parent $L = \frac{1}{3}$.

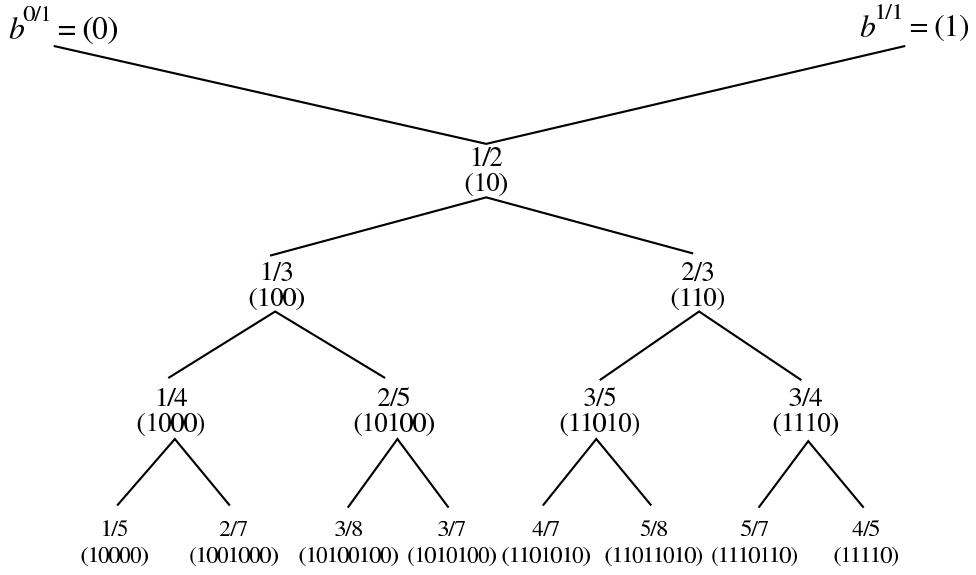

Figure 21: Farey tree for the base $\frac{0}{1}$ and $\frac{1}{1}$ for levels zero to three, and the corresponding b-codes.

Lemma 14. *The canonical velocity code for the Farey daughter of neighbors $\frac{p}{q} < \frac{m}{n}$ is the concatenation of the codes of the parents:*

$$\mathbf{b}\left(\frac{p}{q} \oplus \frac{m}{n}\right) = \mathbf{b}\left(\frac{m}{n}\right)\, \mathbf{b}\left(\frac{p}{q}\right) \ .$$

Proof. Let $\omega = \frac{p+m}{q+n}$ denote the daughter, and $\theta_t = \omega t$. Then $b_t(\omega) = i$ if $\{\theta_t\} \in B_i(\omega)$. We first show that the first n symbols are given by the code for $\frac{m}{n}$, i.e. that $\{\frac{m}{n}t\} \in B_i(\frac{m}{n})$ implies that $\{\theta_t\} \in B_i(\omega)$ for $0 \le t < n$.

Suppose first that $b_t(\frac{m}{n}) = 1$, then there is an integer j such that

$$j - \frac{m}{n} < \frac{m}{n}t \le j \ . \tag{37}$$

Since $\omega < \frac{m}{n}$, the right inequality implies $\omega t \le j$; providing $t \ge 0$. This is the first half of what we desired to show. Since t is an integer, the left inequality in Eq. (37) implies that

$$\frac{m}{n}(t+1) \ge j + \frac{1}{n} \ .$$

Combining this with the relation

$$\omega = \frac{p+m}{q+n} = \frac{m}{n} - \frac{1}{n(q+n)} \ ,$$

implies that

$$\omega(t+1) \ge j + \frac{1}{n} - \frac{t+1}{n(q+n)} > j \ ,$$

providing $t < q+n-1$. Thus we have shown $b_t(\frac{m}{n}) = 1 \implies b_t(\omega) = 1$, for $0 \le t < q+n-1$ (this is more than we needed to prove).

To check that the 0 symbols agree, we must show that when there exists an integer j such that

$$j < \frac{m}{n}t \le j + 1 - \frac{m}{n}$$

then $\{\theta_t\} \in B_0(\omega)$. A calculation similar to the previous one shows that this is true when $0 \le t < q+n$.

So finally we have shown that the symbol sequence $\mathbf{b}(\omega)$ is given by $\mathbf{b}(\frac{m}{n})$ repeated, except for the last symbol.

Similar calculations show that all symbols but the first in $b_t(\omega)$ agree with $b(\frac{p}{q})$, repeated from the end. □

It is easy to see that Lemma 14 is consistent with the codes in the Farey tree in Fig. 21. For example since $b(1/3) = (100)$ and $\mathbf{b}(2/5) = (10100)$, then $\mathbf{b}(3/8) = \mathbf{b}(2/5)\mathbf{b}(1/3) = (10100100)$, and since $\frac{5}{13} = \frac{3}{8} \oplus \frac{2}{5}$, then $\mathbf{b}(5/13) = \mathbf{b}(2/5)\mathbf{b}(3/8) = (1010010100100)$.

Since all numbers can be constructed by Farey paths, Lemma 14 extends for irrational numbers as well:

Corollary 15. *For any ω whose Farey path includes a parent rational $\frac{m}{n} > \omega$, the first n symbols of $b(\omega)$ are those of $b(\frac{m}{n})$.*

Thus, for example the first 34 symbols in the code for γ^{-2} are given by those of its upper Farey neighbor, $\frac{13}{34}$, whose code can be constructed by concatenation:

$$\begin{aligned} b(13/34) &= b(5/13)b(8/21) = b(5/13)b(5/13)b(3/8) \\ &= b(2/5)b(3/8)b(2/5)b(3/8)b(3/8) = \ldots \\ &= (1010010100100101001010010010100100) \ . \end{aligned}$$

A.3 Acceleration Codes

The acceleration code is defined to be the magnitude of the first difference of the velocity code

$$c_t = |b_t - b_{t-1}| \,. \tag{38}$$

This is well defined only for orbits with $0 \le \omega < \frac{1}{2}$. It could also be called a "same-different" or "exclusive-or" code, since $c_t = 0$ if the velocities are the same and 1 if the velocity changes. The point is that for $\omega < \frac{1}{2}$, there is a one-to-one correspondence between allowed b and acceleration codes because the b-code can never have two or more consecutive 1 symbols, thus we obtain $c_t = 0$ only for the case of a double 0 in the b code.

The acceleration code can be obtained geometrically by defining the sectors $C_1(\omega) = (-\omega, \omega]$ and $C_1(\omega) = (\omega, 1-\omega]$, so that $c_t = i$ when $\{\omega t + \alpha\} \in C_i(\omega)$. This follows because we obtain $c_t = 1$ whenever $b_t = 1$ or $b_{t-1} = 1$. The canonical b-code can be reconstructed from the canonical acceleration code by using the initial condition $b_0 = 1$.

The geometrical construction shows that the symbol 1 always appears doubled in the acceleration code. Moreover, if $m = \lfloor \omega^{-1} \rfloor$, then the acceleration code consists of blocks of the form 110^{m-2} and 110^{m-1}. The acceleration code inherits properties of the b-code.

Corollary 16. *The acceleration code for a rational ω is independent of the phase α.*

Corollary 17. *The canonical acceleration code for a Farey-daughter is the concatenation of the codes for its parents.*

Proof. This follows from Lemma 14, and the fact that the first symbol in the b code is always 1 and the last is always 0. Thus concatenation does not disturb the calculation of the acceleration code symbols. □

The interiors of the sectors $C_i(\omega)$ are identical to the interiors of the wedges $W_i(\omega)$ that define the s-code in §3. Recall that hyperbolic codes were those in the interior of the W_i. Thus if we translate 0 and 1 into + and − appropriately, the acceleration and s-codes are identical for hyperbolic orbits.

Lemma 18. *If we set $s_t = \mathrm{sgn}(2c_t - 1)$, then the acceleration code for an orbit of rotation number ω becomes the hyperbolic s-code.*

For example, since the $\frac{1}{3}$ hyperbolic orbit has acceleration code $(110)^\infty$, the corresponding hyperbolic orbit for the Hénon map has s-code $(--+)^\infty$. The elliptic $\frac{1}{3}$ orbit has code $(-++)^\infty$, obtained as usual by flipping the second symbol in the canonically ordered hyperbolic code; however, the elliptic codes do not arise directly from the twist map acceleration code.

B Substitution Rules

An alternative code for rotational orbits is given by the Farey-substitution rule. This code has been used for monotone circle maps [3], and turns out to be identical to the b-code.

A substitution rule acts on a symbol sequence $\mathbf{s}$ by replacing each symbol with a new sequence. Supposing that $\mathbf{s} \in \{L, R\}^\infty$, we define two substitution operators for left and right transitions:

$$\begin{aligned} F_L(L) &= L\,, \quad F_L(R) = RL \\ F_R(L) &= RL\,, \quad F_R(R) = R\,. \end{aligned} \tag{39}$$

Then the symbol sequence for a number whose Farey path begins at a root with symbol sequence s, is determined by applying the substitution operators in the same sequence. Thus, since 2/7 has Farey path LLR starting at 1/2 whose symbol sequence is (RL), the b code for 2/7 is

$$F_L F_L F_R(RL) = F_L F_L(RRL) = F_L(RLRLL) = RLLRLLL\ .$$

Note that this operation is associative, i.e. the above could also be read as

$$F_L F_L F_R(RL) = F_L F_L F_R(R) F_L F_L F_R(L) = F_L F_L(R) F_L F_L(RL) = F_L F_L(R) F_L F_L(R) L = \ldots$$

Lemma 19. *The canonical hyperbolic b-code for a frequency ω is given by applying the substitution rule for its Farey path with the translation $L \equiv 0$ and $R \equiv 1$.*

Proof. As shown in Lemma 14, the canonical b-code for a Farey daughter is obtained by concatenation of the codes its parents. We will show that this concatenation rule is also valid for the Farey-substitution rule. Combining this with the fact that the code for $\frac{1}{2}$ is $RL = 10$, gives the result.

As discussed in Appendix A.2, the Farey paths for the two parents are obtained by truncating the path of the daughter by removing the last symbol, and all of the repeated last symbols plus one more, respectively. Thus there are two possible cases. First if the path for the daughter is WRL^n for an arbitrary sequence W and $n \geq 1$, then we must show the concatenation rule

$$WRL^n = W \oplus WRL^{n-1}\ .$$

Translating this into substitutions applied to the root (RL), and using the associative property, we obtain

$$\begin{aligned} F_W F_R F_L^n(RL) &= F_W F_R F_L^{n-1}(RLL) = F_W F_R F_L^{n-1}(RL) W F_R F_L^{n-1}(L) \\ &= F_W F_R F_L^{n-1}(RL) F_W(RL) = (W \oplus WRL^{n-1})\,, \end{aligned}$$

which is what we wanted to show because the $\oplus$ concatenation writes down the code of the right neighbor first. A similar calculation holds in the other case, where the daughter is WLR^n, and we can show

$$WLR^n = WFLR^{n-1} \oplus W\ .$$

□

There are other substitution rules that apply to period doubling, and more generally n-tupling sequences [3]. For example, the doubling substitution rule is

$$L \to LR \quad \text{and} \quad R \to LL$$

Applying this sequence to the sequence of ω gives the sequence for $1/2 : \omega$. Applying this recursively gives the ω bifurcations of any orbit from the period-doubling sequence.

C Symmetries and Codes of the Horseshoe

In this section we give simple geometric construction of the relation between the symbol plane and an idealized phase space for the horseshoe map. This helps to visualize the relation between the symmetry lines and the symmetries present in the symbolic codes. Instead of the standard

smooth horseshoe map, we will use a discontinuous, area-preserving horseshoe map that is defined everywhere on the square $[-1,1]$ except for the y axis:

$$H(x,y) = \begin{cases} (-2x-1, -\frac{1}{2}(1+y)) \,, & x<0 \\ (2x-1, \frac{1}{2}(1+y)) \,, & x>0 \end{cases} ,$$

see Fig. 22. The region $x<0$ corresponds to the symbol $.-$, and $x>0$ to $+$. Thus the fixed points of H are $(+)^\infty = (1,1)$, and $(-)^\infty = (-\frac{1}{3}, -\frac{1}{3})$.

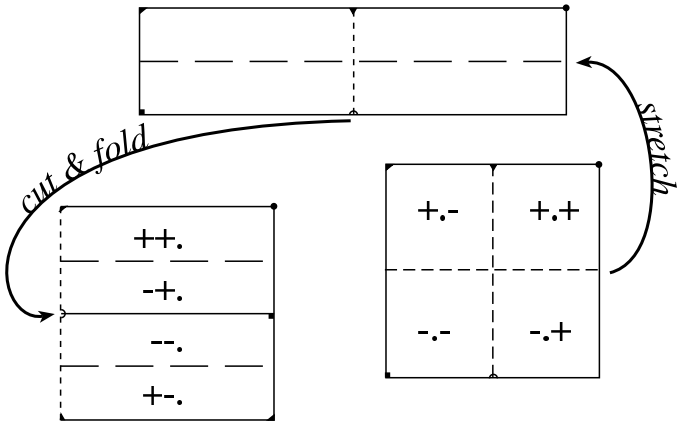

Figure 22: Idealized, discontinuous horseshoe map.

This horseshoe map is reversible, with symmetry $S(x,y) = (y,x)$. As such, it can be factored as $H = RS$, where

$$R = HS = \begin{cases} (-2y-1, -\frac{1}{2}(1+x)) \,, & y<0 \\ (2y-1, \frac{1}{2}(1+x)) \,, & y>0 \end{cases} .$$

Thus the fixed set of R is given by $\mathcal{R} = \{y = -\frac{1}{2}(1+x) : y<0\} \cup \{y = \frac{1}{2}(1+x) : y>0\}$. Alternatively, we can factor $H = ST$ as

$$T = SH = \begin{cases} (-\frac{1}{2}(1+y), -2x-1) \,, & x<0 \\ (\frac{1}{2}(1+y), 2x-1) \,, & x>0 \end{cases} ,$$

with a fixed set $\mathcal{T} = \{y = -2x-1 : x<0\} \cup \{y = 2x-1 : x>0\}$. As usual, we divide the symmetry lines into rays at the "elliptic" fixed point $(-)^\infty$, with the subscript i denoting the rays that lead to the hyperbolic point and o those that lead away, see Fig. 23.

We also show in Fig. 23, the period-two point $(-.+)^\infty = (\frac{1}{5}, -\frac{3}{5})$ and its image $(+.-)^\infty = (-\frac{3}{5}, \frac{1}{5})$. Note that these points lie on $\mathcal{T}_i$ and $\mathcal{T}_o$, respectively, in accord with Table 2 since $H\mathcal{T}_o = \mathcal{R}_o$. Similarly, the elliptic period 3 orbit has points $(-+.+)^\infty = (\frac{1}{9}, \frac{1}{9}) \in \mathcal{S}_i$, $(++.-)^\infty = (-\frac{7}{9}, \frac{5}{9}) \in \mathcal{T}_o$, and $(+-.+)^\infty = (\frac{5}{9}, -\frac{7}{9})$. The hyperbolic period 3 orbit has points $(--.+)^\infty = (\frac{3}{7}, -\frac{1}{7}) \in \mathcal{T}_i$, $(-+.-)^\infty = (-\frac{1}{7}, \frac{3}{7})$, and $(+-.-)^\infty = (-\frac{5}{7}, -\frac{5}{7}) \in \mathcal{S}_o$.

We can divide the symmetry lines into rays at the $(-)^\infty$ fixed point. Note that points with x larger than that for the elliptic fixed point will be on the ray that goes to the hyperbolic point (labeled i), and those with x smaller will be on the ray o. A standard result gives us the ordering.

Lemma 20 (Ordering (c.f. [3, §2.3.2])). *Suppose two symbol sequences* $\mathbf{s} = .s_0 s_1 s_2 \ldots$ *and* $\mathbf{s}'$ *agree for their first* j *symbols, but that* $s_j \neq s'_j$. *Then the corresponding points* x *and* x' *on*

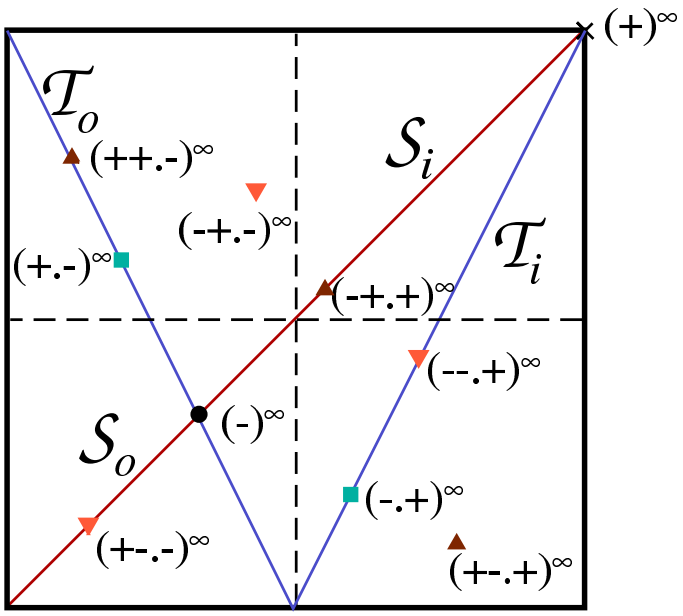

Figure 23: Symmetry lines and periodic orbits of the discontinuous horseshoe. The two fixed points are shown as a circle and x, the period-two points as squares, and the points on the two period-three orbits as triangles.

the horseshoe are ordered as $x < x'$ if the parity, Eq. (6), of $s_0 s_1 \ldots s_j$ is odd (and hence that of $s_0 s_1 \ldots s'_j$ is even).

Thus sequences are ordered the same as their parities. This implies that symbol sequences for the symmetry rays are distinguished by "odd" or "even" blocks of $-$ symbols after the binary point, see Eq. (21).

References

[1] D. A. Lind and B. Marcus. *An Introduction to Symbolic Dynamics and Coding*. Cambridge University Press, Cambridge, 1995.

[2] B.P. Kitchens. *Symbolic Dynamics*. Springer-Verlag, Berlin, 1998.

[3] Bai-Lin Hao and Wei-Mou Zheng. *Applied Symbolic Dynamics and Chaos*, volume 7. World Scientific Publishing Co. Inc., River Edge, NJ, 1998.

[4] D. Sterling, H.R. Dullin, and J.D. Meiss. Homoclinic bifurcations for the Hénon map. *Physica D*, 134:153–184, 1999.

[5] M. Hénon. Numerical study of quadratic area-preserving mappings. *Quart. Appl. Math.*, 27:291–312, 1969.

[6] S. Aubry and G. Abramovici. Chaotic trajectories in the standard map, the concept of anti-integrability. *Physica D*, 43:199–219, 1990.

[7] A. N. Sarkovskii. Coexistence of cycles of a continuous map of a line into itself. *Ukr. Mat. Z.*, 16:61–71, 1964.

[8] N. Metropolis, M. L. Stein, and P. R. Stein. On finite limit sets for transformations of the unit interval. *J. of Combinatorial Theory*, 15(1):25–44, 1973.

[9] M. Hénon. A two-dimensional mapping with a strange attractor. *Comm. Math. Phys*, 50(1):69–77, 1976.

[10] P. Grassberger and H. Kantz. Generating partitions for the dissipative Hénon map. *Phys. Lett. A*, 113(5):235–238, 1985.

[11] P. Cvitanovic, G.H. Gunaratne, and I. Procaccia. Topological and metric properties of Hénon-type strange attractors. *Physical Review A*, 38(3):1503–1520, 1988.

[12] K.T. Hansen. Remarks on the symbolic dynamics for the Hénon map. *Phys. Lett. A*, 165:100–104, 1992.

[13] F. Giovannini and A. Politi. Generating partitions in Hénon-type maps. *Phys. Lett. A*, 161:332–336, 1992.

[14] H.P. Fang. Dynamics for a two-dimensional antisymmetric map. *J. Phys. A*, 27:5187–5200, 1994.

[15] O. Biham and W. Wenzel. Characterization of unstable periodic orbits in chaotic attractors and repellers. *Phys. Rev. Lett.*, 63:819–822, 1989.

[16] D. Sterling and J.D. Meiss. Computing periodic orbits using the anti-integrable limit. *Physics Letters A*, 241:46–52, 1998.

[17] P. Grassberger, H. Kantz, and U. Moenig. On the symbolic dynamics of the Hénon map. *J Phys A*, 22(24):5217–5230, 1989.

[18] K. T. Hansen and P. Cvitanovic. Bifurcation structures in maps of Hénon type. *Nonlinearity*, 11(5):1233–1261, 1998.

[19] F. Christiansen and A. Politi. Generating partition for the standard map. *Physical Review E*, 51:R3811–R3814, 1995.

[20] F. Christiansen and A. Politi. Guidelines for the construction of a generating parition in the standard map. *Physica D*, 109:32–41, 1997.

[21] F. Christiansen and A. Politi. Symbolic encoding in symplectic maps. *Nonlinearity*, 9:1623–1640, 1996.

[22] P. Veerman. Symbolic dynamics and rotation numbers. *Phys. A*, 134(3):543–576, 1986.

[23] Wei-Mou Zheng. Symbolic dynamics for the circle map. *Int. J. Mod. Phys. B*, 5:481–495, 1991.

[24] I.C. Percival and F. Vivaldi. A linear code for the sawtooth and cat maps. *Physica D*, 27:373–386, 1987.

[25] J.D. Meiss. Class renormalization: Islands around islands. *Phys. Rev. A*, 34(3):2375–2383, 1986.

[26] Y. Aizawa. Symbolic dynamics approach to the two-D chaos in area-preserving maps. *Prog. Theor. Phys.*, 71:1419–1421, 1984.

[27] V. Afraimovich, A. Maass, and J. Uras. Symbolic dynamics for sticky sets in Hamiltonian systems. *Nonlinearity*, 13:617–637, 2000.

[28] J.D. Meiss and E. Ott. Markov tree model of transport in area preserving maps. *Physica D*, 20:387–402, 1986. A.P. maps, boundary circles, islands around islands.

[29] R.S. MacKay. *Renormalisation in Area-Preserving Maps*, volume 6 of *Advanced Series in Nonlinear Dynamics*. World Scientific, Singapore, 1993.

[30] J.D. Meiss. Symplectic maps, variational principles, and transport. *Reviews of Modern Physics*, 64(3):795–848, 1992.

[31] H.R. Dullin, J.D. Meiss, and D. Sterling. Generic twistless bifurcations. *Nonlinearity*, 13:203–224, 1999.

[32] R.L. Devaney and Z. Nitecki. Shift automorphisms in the Hénon mapping. *Commun. Math. Phys.*, 67:137–146, 1979.

[33] S. J. Aubry. The concept of anti-integrability: Definition, theorems and applications to the standard map. *Twist Mappings and Their Applications, Ed Richard McGehee, Kenneth R. Meyer*, pages 7–54, 1992.

[34] K.R. Meyer and G.R. Hall. *Introduction to the Theory of Hamiltonian Systems*, volume 90 of *Applied Mathematical Sciences*. Springer-Verlag, New York, 1992.

[35] J. Franks. Periodic points and rotation numbers for area-preserving diffeomorphisms of the plane. *Publications Mathématiques De l'IHÉS*, 71:105–120, 1990.

[36] J.K. Moser. On quadratic symplectic mappings. *Math. Zeitschrift*, 216:417–430, 1994.

[37] S. Aubry and P.Y. Le Daeron. The discrete Frenkel-Kontorova model and its extensions. *Physica D*, 8:381–422, 1983.

[38] A. Backer and H.R. Dullin. Symbolic dynamics and periodic orbits for the cardioid billiard. *Journal of Physics A*, 30(6):1991–2020, 1997.

[39] H.R. Dullin, D. Sterling, and J.D. Meiss. Self-rotation number using the turning angle. *Physica D*, 145(1-2):25–46, 2000.

[40] D. Sterling. *Anti-Integrable Continuation and the Destruction of Chaos.* PhD Thesis, University of Colorado, 1999.

[41] J.W.S. Lamb and J.A.G. Roberts. Time-reversal symmetry in dynamical systems: A survey. *Physica D*, 112:1–39, 1998.

[42] J.J.P. Veerman and F.M. Tangerman. Intersection properties of invariant manifolds in certain twist maps. *Communications in Mathematical Physics*, 139:245–265, 1991.

[43] A. Gómez and J.D. Meiss. Reversors and symmetries for polynomial automorphisms of the complex plane. *Nonlinearity*, 17:975–1000, 2004.

[44] I.C. Percival and F. Vivaldi. Arithmetical properties of strongly chaotic motion. *Physica D*, 25:105–130, 1987.

[45] Q. Chen, J.D Meiss, and I.C Percival. Orbit extension methods for finding unstable orbits. *Physica D*, 29:143–154, 1987.

[46] Q. Chen, I. Dana, J.D. Meiss, N. Murray, and I.C. Percival. Resonances and transport in the sawtooth map. *Physica D*, 46:217–240, 1990.

[47] G.H. Hardy and E.M. Wright. *An Introduction to the Theory of Numbers.* Oxford Univ. Press, Oxford, 1979. Theorem 25.